NeuroImage 247 (2022) 118832

Contents lists available at ScienceDirect

NeuroImage

journal homepage: www.elsevier.com/locate/neuroimage

Finding the best clearing approach - Towards 3D wide-scale multimodal imaging of aged human brain tissue

Henriette Rusch[a], Malte Brammerloh[b,c,d], Jens Stieler[a], Mandy Sonntag[a], Siawoosh Mohammadi[b,e], Nikolaus Weiskopf[b,c], Thomas Arendt[a], Evgeniya Kirilina[b,f], Markus Morawski[a,b,*]

[a] Paul Flechsig Institute of Brain Research, Medical Faculty, University of Leipzig, Liebigstraße 19, Leipzig 04103, Germany
[b] Department of Neurophysics, Max Planck Institute for Human Cognitive and Brain Science, Stephanstraße 1a, Leipzig 04103, Germany
[c] Felix Bloch Institute for Solid State Physics, Faculty of Physics and Earth Sciences, University of Leipzig, Linnéstraße 5, Leipzig 04103, Germany
[d] International Max Planck Research School on Neuroscience of Communication: Function, Structure, and Plasticity, Stephanstraße 1a, Leipzig 04103, Germany
[e] Institute of Systems Neuroscience, University Medical Center Hamburg-Eppendorf, Martinistraße 52, Hamburg 20246, Germany
[f] Center for Cognitive Neuroscience Berlin, Free University Berlin, Habelschwerdter Allee 45, Berlin 14195, Germany

ARTICLE INFO

Keywords:
Tissue clearing
CLARITY
IDISCO
Light sheet microscopy
Immunohistochemistry

ABSTRACT

The accessibility of new wide-scale multimodal imaging techniques led to numerous clearing techniques emerging over the last decade. However, clearing mesoscopic-sized blocks of aged human brain tissue remains an extremely challenging task. Homogenizing refractive indices and reducing light absorption and scattering are the foundation of tissue clearing. Due to its dense and highly myelinated nature, especially in white matter, the human brain poses particular challenges to clearing techniques.

Here, we present a comparative study of seven tissue clearing approaches and their impact on aged human brain tissue blocks (> 5 mm). The goal was to identify the most practical and efficient method in regards to macroscopic transparency, brief clearing time, compatibility with immunohistochemical processing and wide-scale multimodal microscopic imaging. We successfully cleared 26 × 26 × 5 mm^3-sized human brain samples with two hydrophilic and two hydrophobic clearing techniques. Optical properties as well as light and antibody penetration depths highly vary between these methods. In addition to finding the best clearing approach, we compared three microscopic imaging setups (the Zeiss Laser Scanning Microscope (LSM) 880 , the Miltenyi Biotec Ultramicroscope II (UM II) and the 3i Marianas LightSheet microscope) regarding optimal imaging of large-scale tissue samples.

We demonstrate that combining the CLARITY technique (Clear Lipid-exchanged Acrylamide-hybridized Rigid Imaging compatible Tissue hYdrogel) with the Zeiss LSM 880 and combining the iDISCO technique (immunolabeling-enabled three-dimensional imaging of solvent-cleared organs) with the Miltenyi Biotec UM II are the most practical and efficient approaches to sufficiently clear aged human brain tissue and generate 3D microscopic images. Our results point out challenges that arise from seven clearing and three imaging techniques applied to non-standardized tissue samples such as aged human brain tissue.

Abbreviations: AF, autofluorescence; Ce3D, clearing-enhanced 3D microscopy; CLARITY, Clear Lipid-exchanged Acrylamide-hybridized Rigid Imaging compatible tissue hYdrogel; CT, computer tomography; CUBIC, Clear, Unobstructed Brain/Body Imaging Cocktails and Computational analysis; DBE, dibenzylether; DCM, dichloromethane; diSPIM, dual inverted selective plane illumination microscope; dMRI, diffusion-weighted MRI; DP, detection plane; ECi, ethylcinnamate; FOV, field of view; fps, frame per second; GFAP, glial fibrillary acidic protein; GM, gray matter; iDISCO, immunolabeling-enabled three-dimensional imaging of solvent-cleared organs; IP, illumination plane; LSM, confocal laser scanning microscope; LSFM, light sheet fluorescence microscopy; MASH, Multiscale Architectonic Staining of Human cortex; MBP, myelin basic protein; MRI, magnetic resonance imaging; NA, numerical aperture; PET, positron emission tomography; PLP, proteolipid protein; PMD, *post mortem* delay; RI, refractive index; RIMS, RI matching solution; SDS, sodium dodecyl sulfate; TDE, thiodiethanol; TM, transmission; UM II, Ultramicroscope II; UV, ultraviolet; WD, working distance; WM, white matter.

* Corresponding author.
E-mail address: Markus.Morawski@medizin.uni-leipzig.de (M. Morawski).

https://doi.org/10.1016/j.neuroimage.2021.118832.
Received 14 June 2021; Received in revised form 13 December 2021; Accepted 16 December 2021
Available online 17 December 2021.

1. Introduction

Werner Spalteholz proposed the idea of tissue clearing in 1914, which has seen a revival one hundred years later due to new clearing methods (Chung et al., 2013) and large-scale microscopic imaging techniques such as ultramicroscopy and light-sheet microscopy (Dodt et al., 2007). These novel techniques can image mesoscopic tissue blocks (mm-sized) with (sub)cellular resolution. This led to the emergence of numerous clearing techniques over the last decade. Several reviews summarize existing tissue clearing approaches and their biomedical applications (Richardson and Lichtman, 2015; Silvestri et al., 2016; Costantini et al., 2019; Ueda et al., 2020; Tian et al., 2020). Tissue clearing techniques can be categorized into three groups: hydrogel-based, hydrophilic, and hydrophobic techniques. All rely on similar processing steps: i) tissue fixation, ii) permeabilization iii) decolourization, and iv) refractive index (RI) matching (Ueda et al., 2020). The principle behind any tissue clearing is matching the heterogeneous RI of intra- and extracellular compartments divided by lipid membranes, to each other and to the RI of the surrounding medium (Dodt et al., 2007). Thereby, light traveling through the sample is scattered less. Simultaneously reducing light absorption, e.g. by decolorization, leads to transparency of the tissue (Kerker, 1969; Johnsen and Widder, 1999). Available clearing methods use different strategies for homogenizing RI. While aqueous clearing techniques like CLARITY (Chung et al., 2013) and CUBIC (Susaki et al., 2015) wash out lipids by using strong detergents (sodium dodecyl sulfate (SDS) or urea), hydrophobic methods like iDISCO (Renier et al., 2014) and ECi (Klingberg et al., 2017) use organic solvents (dibenzylether (DBE) or ethylcinnamate (ECi)) to dissolve tissue lipids.

The combination of tissue clearing and immunohistochemistry is a highly desired tool for studies of human neuroanatomy in 3D and particularly indispensable for unraveling the human connectome. Investigations of lateral cortical cytoarchitectonic structures such as columns in the cortex (Kaas, 2012) and small subcortical nuclei (Alkemade et al., 2020; Brammerloh et al., 2021) is very challenging with 2D histology. Clearing and immunohistochemically processing mesoscopic-sized human brain tissue blocks promise to reveal the 3D microstructure of axonal fibers providing a missing link between 2D histology and non-invasive imaging techniques (i.e. magnetic resonance imaging (MRI)). Particularly, the 3D reconstruction of fiber tracts potentially provides validation for fiber tractography based on diffusion-weighted MRI (dMRI). This application of tissue clearing is strongly motivated by the emerging demand for validating microstructure-informed tractography and *in-vivo* histology using MRI (Morawski et al., 2018; Edwards et al., 2018; Weiskopf et al., 2021). Hence, this study aims at making tissue clearing of aged human brain tissue more accessible to less-related fields of research.

However, clearing mesoscopic-sized blocks of *post mortem* human brain tissue remains a demanding task. There are only few studies on clearing human brain tissue. Moreover, performing immunohistochemistry on cleared human brain tissue appears to be particularly challenging. Small slabs (500 µm thick) of human frontal cortex were cleared and immunohistochemically processed by Chung et al. in 2013 when CLARITY was first published. Next, a human embryo of the first trimester including its nervous system was cleared with the organic solvent DBE (Belle et al., 2017). Large blocks ($\lesssim$ 8 mm) of human cortex from elderly donors were cleared by using the hydrogel-based CLARITY method, requiring ten months of clearing. In the same study, immunohistochemistry was applied to cleared samples ($\lesssim$ 5 mm) and images of neurons, glia cells and myelinated fibers with (sub)cellular resolution were generated (Morawski et al., 2018). In 2019, Cartmell et al. performed a multi-modal study investigating the human *Nucleus accumbens* (0.5 mm) and its neuropathology combining dMRI with the CLARITY and SWITCH (Murray et al., 2015) tissue clearing techniques. This combination of dMRI and CLARITY continued to be of interest as a tool to verify and interpret lesser resolved dMRI data (Leuze et al., 2021). Simultaneously, the MASH technique was introduced, where dehydration and bleaching steps are combined with hydrophobic clearing (using thiodiethanol (TDE) and trans-cinnamaldehyde) to clear coronal slices (2 – 5 mm) of aged human brain and analyze its cytoarchitecture via histological dyes (Hildebrand et al., 2019). Furthermore, an entire human brain including the eye was rendered transparent using the SHANEL protocol, where CHAPS was introduced as a clearing detergent with higher permeability and smaller micelles that pass faster through human brain tissue than SDS used for CLARITY (Zhao et al., 2019). In summary, although several approaches demonstrated their feasibility, clearing and immunohistochemical processing of aged human brain tissue remains the absolute exception.

Clearing densely packed human brain tissue poses many tissue-specific challenges with experimental duration being the main drawback. Studies of structure and function of the human central nervous system depend massively on donated *post mortem* brain tissue (Stan et al., 2006). With a rare exception of clinical studies on post-operative tissue samples, human brain tissue is collected after the donor's natural death following strict laboratory and ethical standards. In most countries, where such research is performed, the life expectancy is high and mortality in childhood and early adult life is low. Therefore, the majority of *post mortem* studies in humans are performed on brain tissue from donors of high age, referred below as "aged" brain tissue.

Clearing of aged human brain tissue is particularly challenging because of the high, varying donor age leading to increased light scattering within the brain tissue (Duncan et al., 1996) as well as to lipid and protein, e.g. lipofuscin and melanin, accumulation in the sample (Goyal, 1982; Morawski et al., 2004). Other challenging properties of aged human brain tissue are: long and varying *post mortem* delays (PMD) that start autolytic processes of the tissue (Sele et al., 2019); rigid immersion fixation protocols, as perfusing human tissue is challenging for technical and ethical reasons; no influence on genetic modifications (i.e. omission of genetically-induced fluorescence) and high myelin content leading to increased autofluorescence (Monici, 2005). Consequently, these factors need to be considered when designing a clearing protocol for aged human brain tissue.

The goal of this study is to compare the performance of seven promising clearing techniques to find the most practical and efficient technique for aged human brain tissue, that is frequently used in histological and MRI research in humans. Ideally, this clearing technique is faster and capable of higher throughput than CLARITY (Chung et al., 2013), which was proven to work on aged human brain tissue (Morawski et al., 2018). For this study, performance is operationalized as a combination of macroscopic transparency, compatibility with immunohistochemical processing (consistent antibody penetration), and highest achievable microscopic resolution and imaging depth. In order to achieve high inter-methodological variety, we selected tissue clearing methods, which seemed well-established, easy or fast performing, top-notch and transferable to human brain tissue. Based on these prerequisites, the clearing techniques investigated in this study include: CLARITY (Chung et al., 2013) as a hydrogel-based method, CUBIC (Susaki et al., 2015) and Ce3D (Li et al., 2017) as hydrophilic methods and iDISCO (Renier et al., 2014), MASH (Hildebrand et al., 2019), Visikol (Villani et al., 2013), and ECi (Klingberg et al., 2017) as hydrophobic methods with Visikol being a commercial tissue clearing kit. All methods have been tested on rodent and human tissue (CLARITY: Ando et al., 2014, Liu et al., 2016; CUBIC: Nojima et al., 2017, Kubota et al., 2017; iDISCO: Renier et al., 2016, Perin et al., 2019; MASH: Hildebrand et al., 2019; Visikol: Merz et al., 2018, Struzyna et al., 2018; ECi: Masselink et al., 2018) except Ce3D, which has been solely tested on rodent tissue so far (Bossolani et al., 2019). This indicates great potential for transferring it to aged human brain tissue. Also, the CLARITY, CUBIC, iDISCO, and MASH methods have been tested on human central nervous tissue (CLARITY: Chung et al., 2013, Costantini et al., 2015, Morawski et al., 2018; CUBIC: Jing et al., 2018; iDISCO: Belle et al., 2017; MASH: Hildebrand et al., 2019) and achieved macroscopic transparency and microscopic resolution. Never-

Table 1
Overview of used samples. Case number, age, *post mortem* delay (PMD) and region of interest (ROI) of donor brains used for respective clearing technique and in different experiments. Figures displaying these ROI are given as well. GC: *Gyrus cinguli*; OC: *Chiasma opticum*; CR: *Corona radiata*; MO: *Medulla oblongata*; MaA: Macroscopic assessment; OP: Optical Properties; MiA: Microscopic assessment of immunohistochemistry; PD: Penetration depth; CMS: Comparison of microscopic setup; * with *Corpus callosum*; ° without *Corpus callosum*.

CASE NR.	AGE	PMD	USED ROI	APPLIED PROTOCOL	THICKNESS [MM]	EXPERIMENT	FIGURE
1	63 yrs	20 h	a: GC*	CLARITY	5	MaA; OP	1; 2; 3
			b: GC*	CUBIC	5	MaA; OP	1; 2; 3
			c: GC*	MASH	2,5	MaA; OP	1; 2; 3
			d: GC*	Visikol	5	MaA; OP	1; 2; 3
			e: GC*	Ce3D	5	MaA; OP	1; 2; 3
2	61 yrs	18 h	a: GC°	iDISCO	5	MaA; OP	1; 2; 3
			b: GC°	ECi	5	MaA; OP	1; 2; 3
3	59 yrs	48 h	OC	CLARITY	6	MiA; PD	4; 5
4	89 yrs	24 h	a: CR	CLARITY	0,3	CMS	6
			b: MO	iDISCO	2,5	MiA; PD	4; 5

theless, neither of these studies achieved the combination of quickly attained high transparency, immunohistochemical processing, and high microscopic resolution in mesoscopic blocks of aged human brain tissue. Hence, this study aims at accelerating the clearing process, increasing sample thickness (~ 5 mm), performing immunohistochemical processing and microscopic imaging on *post mortem* aged human brain tissue. This is achieved by a systematic comparison of seven different clearing techniques in combination with three microscopic imaging setups, illustrating several pitfalls and limitations of clearing and immunohistochemical processing of aged human brain tissue.

2. Materials and methods

2.1. *Collection and preparation of aged* post mortem *human brain tissue*

Brains (4 cases, m/f; age: Ø 68 yrs ± 10.5; PMD Ø 25 *h* ± 10.25 h) (Table 1) were provided by the Body donation program, Institute of Anatomy, Medical Faculty, University of Leipzig, the Brain Banking center Leipzig of the German Brain-Net, operated by the Paul Flechsig Institute of Brain Research, Medical Faculty, University of Leipzig and the Department of Neuropathology, Medical Faculty, University of Leipzig. The entire procedure of case recruitment, acquisition of the patient's personal data, the protocols and the informed consent forms, performing the autopsy, and handling the autopsy material have been approved by the responsible authorities (Approval by the Sächsisches Bestattungsgesetz von 1994, 3. Abschnitt, §18, Ziffer 8; GZ 01GI9999–01GI0299; Approval # WF-74/16, Approval # 282–02 and Approval # 205/17-ek). Neuropathological assessment revealed no signs of any neurological diseases. The PMD prior to fixation varied between 18 and 48 h. Following the standard Brain Bank procedures, samples were immersion-fixed in either 3% paraformaldehyde (PFA) and 1% glutaraldehyde (GA) or 4% PFA in phosphate-buffered saline (PBS) (pH 7.4) for at least 6 weeks. Samples of *Gyri cinguli* are separate pieces from two coronal slices of human cerebrum (case 1, 2) either with or without parts of the *Corpus callosum*. Remaining regions of interest include *Optic chiasm* (case 3), *Medulla oblongata* (case 4) and *Corona radiata* (case 4), all stemming from different donors.

2.2. *Clearing*

CLARITY

Samples were cleared following Chung et al., 2013, modified according to Morawski et al., 2018 and Costantini et al., 2015. After fixation, three tissue blocks sized from ~ 25 × 25 × 5 mm^3 to 40 × 40 × 0.3 mm^3 (ROI 1a, 3, 4a; Table 1) were washed in PBS and incubated in a hydrogel solution, which was exsiccated and polymerized after 2 weeks. The samples were passively incubated in SDS-based clearing solution (4% SDS, in 200 mM boric acid, pH 8.5) for up to 2 weeks at 37 °C. The samples were transferred into customized electrophoretic chamber (Biostep GmbH, Jahnsdorf, Germany) using 5 V and 1.6 A at 40 °C for active clearing for 4 - 16 months. After immunohistochemical processing, samples were optically cleared in 63% thiodiethanol (TDE, RI = 1.45). For imaging, the sample was embedded in 1.5% low-melting agarose in 63% TDE to minimize vibrations during imaging.

CUBIC

The sample (1b; Table 1) was cleared following Susaki et al., 2015. After fixation, a tissue block sized 25 × 25 × 5 mm^3 incubated in diluted Reagent 1 (10% urea, 10% Triton X-100, 5% Quadrol in A.d., 25 mM NaCl, degassed at 100 mbar for ~ 30 min) for ≥ 6 h The sample was transferred into Reagent 1 for 5 months. After immunohistochemical processing, sample was optically cleared with 50% Reagent 2 with RI = 1.48 (25% urea, 50% sucrose and 10% triethanolamine in A.d.). For imaging, sample was embedded in 1.5% low-melting agarose in PBS-NaN_3 to minimize sample vibrations.

iDISCO

Samples were cleared following Renier et al., 2014. After fixation, tissue blocks sized 25 × 25 × 5 mm^3 were dehydrated in an ascending MeOH-PBS series (50%, 80%, 100%). Samples were bleached and rehydrated the following day using the same MeOH-PBS steps. Clearing was performed after immunohistochemical processing starting with dehydration in an ascending MeOH-PBS series (20%, 40%, 60%, 80%, 100%, 100%). Next, samples were incubated in 66% dichloromethane (DCM) and 33% MeOH for 3 h or overnight. Subsequently, samples were incubated in 100% DCM until equilibration and eventually transferred into 100% dibenzylether (DBE; RI = 1.56) for optical clearing.

MASH

The sample was cleared following Hildebrand et al., 2019. After fixation, tissue block sized 25 × 25 × 2.5 mm^3 was dehydrated in an ascending MeOH-PBS series (20%, 40%, 60%, 80%, 100%, 100%). Next, sample was bleached overnight and rehydrated (80%, 60%, 40%, 20%). Clearing was performed after immunohistochemical processing starting with dehydration in an ascending MeOH-PBS series (20%, 40%, 60%, 80%, 100%, 100%). Subsequently, sample was incubated in 66% DCM and 33% MeOH for 3 h or overnight. Subsequently, sample was incubated in 100% DCM until equilibration (ON) and eventually transferred into 62% TDE and 38% trans-cinnamaldehyde (RI matching solution) with RI = 1.56.

Visikol

The sample was cleared following a clearing protocol created with Visikol online protocol builder (last viewed 07/18). The tissue block (25 × 25 × 5 mm^3) was incubated in permeabilization buffer and afterwards immersed in 20%, 80%, 100% MeOH-PBS. It was incubated in 20% DMSO-MeOH twice and rehydrated in 80% and 50% MeOH-PBS. After washing sample was incubated in penetration buffer (0.2% Triton X-100, 2.25% glycine, 20% DMSO in PBS). Clearing was performed after immunohistochemical processing starting with dehydration in ascend-

ing MeOH-PBS series (50%, 70%, 100%). Next, the sample was incubated in HISTO-1 for 1 d at RT and transferred into HISTO-2 eventually. Sample remained in optical clearing medium (HISTO-2) with RI = 1.53 for ≥ 3 months to potentially reach transparency.

ECi

The sample was cleared following Klingberg et al., 2017. After immunohistochemistry, a tissue block sized 25 × 25 × 5 mm^3 was immersed in ascending EtOH-A.d. series (30%, 50%, 70%, 100%, 100%) and 2% Tween. Next, the sample was incubated in Ethylcinnamate (ECi) with RI = 1.56 and remained in optical clearing medium (ECi) for ≥ 3 months to potentially reach transparency.

Ce3D

The sample was cleared according to Li et al., 2017. After immunohistochemistry, tissue block sized 25 × 25 × 5 mm^3 was immersed in clearing solution with RI = 1.56 (40% v/v N-methylacetamide, 86% w/v Histodenz™, 0.1% v/v Triton X-100, 0.5% v/v thioglycerol in PBS). Sample remained in clearing solution for ≥ 3 months to potentially reach transparency.

For a more detailed description of all clearing methods, please see the Supplementary Information.

2.3. Immunohistochemistry

CLARITY

Samples were immunohistochemically processed after active clearing. The procedure has been modified according to Cartmell et al., 2019; Murray et al., 2015. For triple fluorescent staining, samples were incubated in primary antibodies (Supplementary Information Table S1) in PBS-Triton X-100 (0.2%) in 1 mM SDS-PBS solution. Primary antibodies included tubulin marker (anti-β-lll-tubulin, rabbit, 1:500), myelin marker (anti-myelin basic protein, rat, 1:400) and lipid marker (anti-proteolipid protein, mouse, 1:250). Incubation in secondary antibody in PBS-Triton X-100 in 1 mM SDS-PBS followed. Secondary antibodies included Donkey-anti-rabbit Cy2 (1:800), Donkey-anti-rat Cy3 (1:800) and Donkey-anti-mouse Cy5 (1:500), all from Dianova, Hamburg, Germany.

CUBIC

Sample was immunohistochemically processed after clearing. The procedure has been modified according to Morawski et al., 2018. The sample was immersed in blocking solution (2% BSA, 0.3% milk powder, 0.5% DNS, 0.1% NaN_3 in 0.02% PBS-Tween 20) followed by triple fluorescent staining by incubation in primary antibody (Supplementary Information Table S1) solution. Primary antibodies included tubulin marker (anti-β-lll-tubulin, rat, 1:1000), myelin marker (anti-myelin basic protein, rat, 1:400) and neuronal marker (anti-human neuronal protein C/D, mouse, 1:400). Sample was incubated in secondary antibody solution including Donkey-anti-rabbit Cy2 (1:800), Donkey-anti-rat Cy3 (1:800) and Donkey-anti-mouse Cy5 (1:500), all from Dianova, Hamburg, Germany.

iDISCO

Samples were immunohistochemically processed after pre-treatment steps (dehydration, bleaching, rehydration) and before clearing. The procedure has been modified according to Renier et al., 2016. A PBSGT-stock was prepared consisting of 10X PBS, 0.2% gelatin, 0.5% Triton X-100 and 0.1% NaN_3. For triple fluorescent staining, samples were incubated in primary antibodies (Supplementary Information Table S1) in PBSGT + 0.1% saponin. Primary antibodies included tubulin marker (anti-β-lll-Tubulin, rabbit, 1:1000), myelin marker (anti-MBP, rat, 1:400; anti-PLP, mouse, 1:250) and neuronal marker (anti-human neuronal protein C/D, mouse, 1:400). Samples were incubated in secondary antibodies in PBSGT + 0.1% saponin. Secondary antibodies included Donkey-anti-rabbit Cy2 (1:800), Donkey-anti-rat Cy3 (1:800), Donkey-anti-mouse Cy5 (1:500) and Donkey-anti-rat Cy7 (1:500), all Dianova, Hamburg, Germany.

MASH

The sample was immunohistochemically processed after pre-treatment steps (dehydration, bleaching, rehydration) and before clearing procedure. The procedure has been modified according to Morawski et al., 2018. The sample was incubated in myelin marker (FluoroMyelin™ Red Fluorescent Myelin Stain, 1:300, Life Technologies). Incubation in nuclei marker (DAPI 1:2000) in PBS-NaN_3 followed.

Visikol

The protocol for immunohistochemical processing was created with Visikol online protocol builder (last viewed 07/18). The sample was immersed in blocking solution (2% BSA, 0.3% milk powder, 0.5% DNS, 0.1% NaN_3 in 0.02% PBS-Tween 20) followed by triple fluorescent staining by incubation in primary antibody solution (0.2% Tween 20, 100 µg/ml heparin, 3% DNS, 5%DMSO in PBS). Primary antibodies (Supplementary Information Table S1) included tubulin marker (anti-β-lll-tubulin, rabbit, 1:1000), myelin marker (anti-myelin basic protein, rat, 1:400) and neuronal marker (anti-human neuronal protein C/D, mouse, 1:400). Immersion in secondary antibody solution (0.2% Tween 20, 100 µg/mL heparin, 3% DNS, 5%DMSO in PBS). Secondary antibodies included Donkey-anti-rabbit Cy2 (1:800), Donkey-anti-rat Cy3 (1:800) and Donkey-anti-mouse Cy5 (1:500), all Dianova, Hamburg, Germany.

ECi and Ce3D

Samples were immunohistochemically processed before clearing. The procedure was modified according to Renier et al., 2016. A PBSGT-stock was prepared consisting of 10X PBS, 0.2% gelatin, 0.5% Triton X-100 and 0.1% NaN_3. For triple fluorescent staining, samples were incubated in primary antibodies (Supplementary Information Table S1) in PBSGT + 0.1% saponin. Primary antibodies included tubulin marker (anti-β-lll-Tubulin, rabbit, 1:1000), myelin marker (anti-MBP, rat, 1:400; anti-PLP, mouse, 1:250) and neuronal marker (anti-human neuronal protein C/D, mouse, 1:400). Samples were incubated in secondary antibodies in PBSGT + 0.1% saponin. Secondary antibodies included Donkey-anti-rabbit Cy2 (1:800), Donkey-anti-rat Cy3 (1:800), Donkey-anti-mouse Cy5 (1:500) and Donkey-anti-rat Cy7 (1:500), all Dianova, Hamburg, Germany.

For a detailed description of all immunohistochemical processing and used materials, please see the Supplementary Information.

2.4. Imaging

Three microscopic imaging setups were used for 2D and 3D imaging of cleared human brain tissue: a confocal laser scanning microscope and two light sheet microscopes. The Zeiss upright confocal laser-scanning microscope (LSM 880, Carl Zeiss Jena, Jena, Germany) was used for imaging CLARITY-, CUBIC- and MASH-treated samples. Due to highly aggressive imaging medium (organic solvent DBE), the iDISCO-treated sample could not be imaged with this setup. The Zeiss LSM 880 is equipped with a 20x immersion objective (numerical aperture (NA) 1.0, working distance (WD) 5.6 mm, refractive index (RI) 1.38; Clr Plan-Apochromat Carl Zeiss Jena, Jena, Germany). The fluorescence was excited with an argon laser (488 nm, Cy2), 2 HeNe lasers (563 nm, Cy3; 633 nm, Cy5) and UV laser diode (405 nm). The emitted light was collected using three band-pass filters: 505–530 nm for Cy2, 565–615 nm for Cy3 and 650–710 nm for Cy5.

The Miltenyi BioTec light sheet fluorescence microscope (UltraMicroscope II, Miltenyi BioTec, Bielefeld, Germany) was used for imaging CLARITY- and iDISCO-treated samples. It is equipped with either a zoom body (0.63x – 6.3x) and 2x immersion objective (NA 0.5, WD 10 mm, RI 1.33 – 1.56; Miltenyi Biotec, Bielefeld, Germany) or a fixed body and 12x immersion objective (NA 0.53, WD 10 mm, RI 1.487 – 1.647; Miltenyi Biotec, Bielefeld, Germany) perpendicular to the detection plane. The fluorescence was excited with laser lines of 488 nm wavelength (Cy2), of 561 nm (Cy3), of 640 nm (Cy5), and of 777 nm (Cy7). The emitted light was collected using filters correcting dynamically for 400 nm – 850 nm (chromatic correction). A Neo 5.5 MP sCMOS camera (2560 × 2160

pixels, 100 fps, Andor, Oxford Instruments, Abingdon, GB) was used for detection.

The 3i Marianas LightSheet™ microscope (3i Intelligent Imaging Innovations, Inc., Denver, Colorado, USA) was used for imaging CLARITY-treated samples. It is equipped with two perpendicular 20x objectives (NA 0.5, WD 3.5, RI = 1.33; UMPLFLN Olympus, Olympus K.K., Shinjuku, Tokio, Japan) generating isotropic resolution. The fluorescence was excited with 488 nm laser line (Cy2), 561 nm laser line (Cy3) and 640 nm laser line (Cy5). A UV laser for detecting 405 nm was also available. Two CMOS cameras (2048 × 2048 pixels, 100 fps, ORCA-Flash 4.0 C13440, Hamamatsu, Hamamatsu Photonics K.K., Hamamatsu City, Japan) were used for detection.

2.5. Volume change estimation

Before and after clearing, all seven human brain tissue samples were photographed and measured by using millimeter paper and a macroscopic ruler. Sample volume changes were estimated by approximating the shape of the sample's top side as a trapezoid (Eq. (1)) and assuming a uniform sample deformation (Eq. (2)).

The equations were:

$$A = \frac{(a+c) \times h_{trapezoid}}{2} \tag{1}$$

$$\frac{V_{after\ clearing}}{V_{before\ clearing}} = \left(\frac{A_{after\ clearing}}{A_{before\ clearing}}\right)^{3/2} \tag{2}$$

2.6. Optical properties of cleared aged human brain tissue

Transmission measurement

The light spectra were measured on a UV–VIS SPECORD 40 photometer (Analytic Jena, Jena, Germany). Each sample underwent three cycles of transmission (TM) measurement (340 - 1000 nm). During the measurement, the cuvette was filled with the respective clearing medium, which was used as reference of 100% TM. Mean TM values were calculated according to this sample-specific TM reference and converted to percentage. These percentage TM values of all samples were compared to each other (Fig. 2). Measuring TM values ≥ 50% was defined as a prerequisite for sufficient transparency of the respective clearing method. The transmittance measured for the tissue block cleared with the MASH technique was corrected to account for lower tissue thickness (2.5 mm), as compared to all other samples (5 mm) using Lambert Beer law. The transmittance values for the MASH-treated sample were squared to scale them to a slab with the doubled thickness (according to Eq. (3) $T_{corr}=e^{5mm*\log(T)/2.5mm}=e^{2*\log(T)}=T^2$).

Transmittance of the tissue samples

The light transmittance of biological tissue at wavelength λ is determined by tissue absorption coefficient $\mu_a(\lambda)$ and tissue reduced scattering coefficients $\mu_s'(\lambda)$, which are both wavelength-dependent. In case of a thin tissue slabs or for low scattering media the total light transmittance T is described by the modified Lambert Beer law:

$$T = e^{-\mu_{eff}(\lambda)L} = e^{-(\mu_s'(\lambda)+\mu_a(\lambda))L} \tag{3}$$

Where $\mu_{eff}(\lambda)$ is an effective absorption coefficient, which, in this case, can be approximated by the sum of absorption and reduced scattering coefficients. This approximation holds if the slab thickness L is smaller or comparable to the averaged light scattering length $(\mu_s'(\lambda))^{-1}$ $(L \leq (\mu_s'(\lambda))^{-1})$.

The tissue reduced scattering coefficient μ_s'

The wavelength dependence of reduced scattering coefficient $\mu_s'(\lambda)$ in most biological tissues is well described by the sum of two separate contributions resulting from Rayleigh and Mie scattering (Jacques, 2013; Tuchin, 2015):

$$\mu_s'(\lambda) = a'\left(f_{Ray}\left(\frac{\lambda}{500\ nm}\right)^{-4} + (1-f_{Ray})\left(\frac{\lambda}{500\ nm}\right)^{-b_{Mie}}\right) \tag{4}$$

Where the wavelength λ is normalized to a reference wavelength, 500 nm to yield a dimensionless value. The scaling factor a' is equal to $\mu_s'(500\ nm)$. The wavelength dependence of Rayleigh scattering is described by $(\frac{\lambda}{500\ nm})^{-4}$, while the contribution of Mie scattering is determined by $(\frac{\lambda}{500\ nm})^{-b_{Mie}}$, where b_{Mie} is the Mie scattering power (Jacques, 2013). The coefficient f_{Ray} indicates the fraction of Rayleigh scattering at 500 nm.

The tissue absorption coefficient μa

The tissue absorption coefficient $\mu_a(\lambda)$ is determined by tissue composition and concentration of tissue chromophores. The main chromophores in brain tissue *in vivo* are hemoglobin, cytochrome c oxidase, lipofuscin and melanin (Johansson, 2010). Since hemoglobin and cytochrome c oxidase are washed out during the clearing process, we assumed, that the absorption coefficient of cleared aged human brain tissue is dominated by the remaining concentrations of lipofuscin and melanin, or other chromophores with similar spectra. Based on literature reports (Johansson, 2010; Jacques, 2013), we further assumed that the wavelength dependence of melanin and lipofuscin could be described by:

$$\mu_a(\lambda) = b\left(\left(\frac{\lambda}{500\ nm}\right)^{-n}\right) \tag{5}$$

Where b is a scaling coefficient proportional to the concentration of the chromophores in the tissue.

Substituting wavelength dependencies of absorption and reduced scattering coefficients described by Eq. Eq. (4) and Eq. (5) the wavelength dependence of effective absorption coefficient $\mu_{eff}(\lambda)$ can be described by following equation:

$$\mu_{eff}(\lambda) = -\frac{\ln(T)}{L} = a'\left(\frac{b}{a'}\left(\frac{\lambda}{500\ nm}\right)^{-n} + f_{Ray}\left(\frac{\lambda}{500\ nm}\right)^{-4} + (1-f_{Ray})\left(\frac{\lambda}{500\ nm}\right)^{-b_{Mie}}\right) \tag{6}$$

We used Eq. (6) to fit experimentally obtained effective absorption coefficients of tissue samples cleared with different clearing technique (Fig. 2). Four fitting parameters were used: *b, n,* f_{Ray} and b_{Mie}. Uncertainties of fitting parameters were determined as a parameter ranges, providing fits with error of fit (square root of sum-of-squares of deviations between fit and experiment) deviating less than 1% from the optimal fit. To visualize relative contribution of absorption and scattering we performed an additional simulation, which separately quantified contributions of absorption (Eq. (5)) and scattering (Eq. (4)) to the overall tissue transmittance, using absorption and scattering coefficients obtained from fitting (Table 2).

3. Results

3.1. Comparing seven clearing techniques on aged post mortem human brain tissue

3.1.1. Macroscopic visual assessments

Each of the seven clearing protocols was applied to an aged *post mortem* human brain tissue sample (4 cases, Ø 68 yrs ± 10.5 yrs, 25 h PMD ± 10.25 h, samples sized ~26 × 18 × 5 mm^3, see Table 1). A comparative macroscopic analysis was performed focusing on tissue transparency, time needed for complete clearing, and volume changes. The tested methods are three hydrophilic (CLARITY, CUBIC, Ce3D) and four hydrophobic clearing techniques (iDISCO, MASH, Visikol, ECi). High transparency is reached when light travels through a tissue with minimal scattering and absorption. We regarded tissue as highly transparent when (i) letters of a text placed underneath a *post mortem* human brain tissue sample were legible (Fig. 1A), (ii) sufficient light transmission (TM) through a 2.5 or 5 mm thick sample was measured (≥ 50%, Fig. 2), and (iii) high quality light microscopy was feasible (Fig. 4). Macroscopic clearing results, i.e. the ability to see letters through the

A

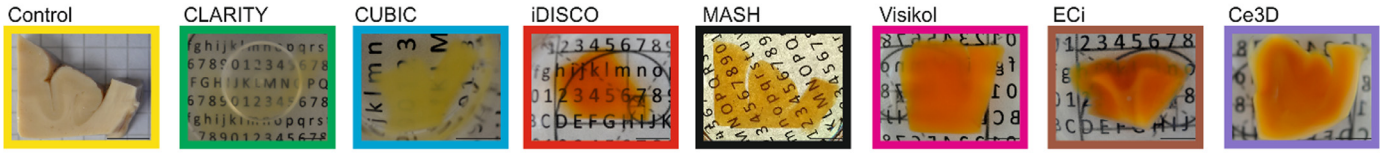

	CLARITY	CUBIC	iDISCO	MASH	Visikol	ECi	Ce3D
visible letters	xx	x	xx	xx	- -	-	- -
blurred letters	x	x	-	- -	n.e.	x	n.e.
sample edges	-	-	-	xx	-	x	-
Δ GM/WM	xx	- -	- -	-	-	x	- -
rigidity	-	-	xx	xx	x	x	x
handling	xx	xx	-	-	x	x	x
deformation	xx	xx	-	-	-	-	x

["xx": strongly/hard, "x": moderate, "-": easily/weak, "- -": not applicable and "n.e.": not evaluated]

B

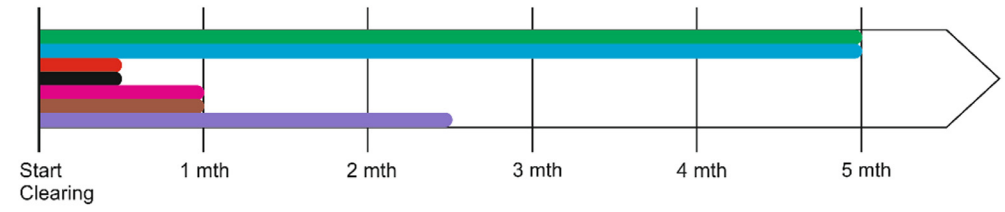

C

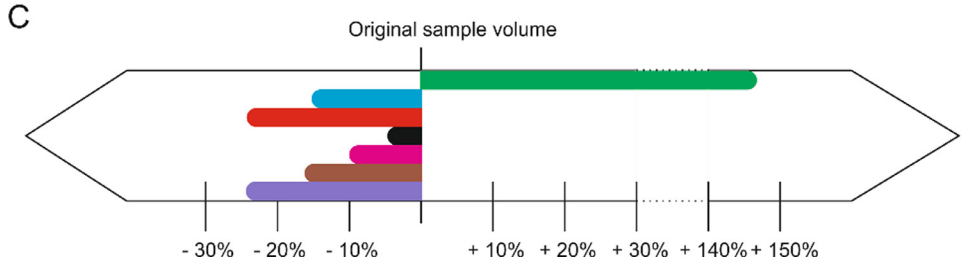

Fig. 1. Macroscopic assessment of seven tissue clearing techniques. (A) Macroscopic results of testing seven different clearing techniques on aged human brain tissue (all *Gyrus cinguli* with/without *Corpus callosum* (samples 1a-e & 2a-b, see Table 1). A *post mortem* PFA-fixed human brain tissue sample (sample 1c before clearing) served as uncleared control (yellow). Scale bar: 1 cm. Transparency has been evaluated by letters becoming legible underneath a *post mortem* human brain tissue sample ("xx": highly legible, "x": partially legible, "-": non-legible), their blurriness ("xx": strongly blurred, "x": partially blurred, "-": not blurred), sharpness of sample edges ("xx": sharp, "x": less sharp, "-": blurred sample edges) and resulting differences between GM and WM (Δ GM/WM with "xx": strong differences, "x": moderate differences, "-": no differences). Also, tissue rigidity ("xx": rigid, "x": semisoft, "-": soft), difficulty to manipulate ("xx": hard to manipulate, "x": moderately manipulatable, "-": easily manipulatable) and overall tissue deformation ("xx": strong deformation, "x": moderate deformation, "-": low deformation) were qualitatively assessed. However, not all properties were applicable ("- -") nor evaluable for all samples ("n.e."). CLARITY- (green), CUBIC- (blue), iDISCO- (red) and MASH-treated (black) samples show underlying letters with blurriness in CLARITY and CUBIC. iDISCO- and MASH-treated sample show sharp letters with MASH-treated sample showing sharp sample edges. In comparison, Visikol- (magenta), ECi- (brown) and Ce3D-treated (violet) samples do not show legible letters, except in GM in the ECi-treated sample. The ECi-treated sample shows sharper sample edges. CLARITY- and CUBIC-treated samples lose rigidity, leading to difficulties in tissue handling. IDISCO- and MASH-treated samples gain rigidity, leading to increased easiness in tissue handling. The changes in tissue rigidity and handling for Visikol-, ECi- and Ce3D-treated samples remain moderate. CLARITY- and CUBIC-treated samples were strongly deformed after clearing, whereas iDISCO-, MASH-, Visikol- and ECi-treated samples demonstrated very low tissue deformations. Moderate deformations were observed for Ce3D-treated sample. (B) Timeline shows the duration of clearing protocols. Hydrophilic methods took several months, whereas hydrophobic methods needed ≤ 1 month, but sufficient transparency was not reached in all cases. In case of insufficient transparency, the durations reported in the literature is displayed. (C) Scheme shows the differences in sample volume [%] of cleared human brain tissue samples compared to the uncleared sample volume. All seven cleared samples show volume changes. The CLARITY-treated sample expanded 146% in volume. The following volume shrinkages occurred using the other investigated techniques: CUBIC: 27%; iDISCO: 24%; MASH: 4%; ECi: 16%; Visikol: 9%; Ce3D: 24%.

Table 2
Optical properties of all tissue samples resulting from fitting the wavelength dependence of the effective tissue absorption coefficient by a combination of Rayleigh and Mie scattering of the tissue and light absorption by melanin and lipofuscin. The equation $\mu_{eff}(\lambda) = -\frac{\ln(T)}{L} = a(b(\frac{\lambda}{500\ nm})^{-n} + f_{Ray}(\frac{\lambda}{500\ nm})^{-4} + (1 - f_{Ray} - b)(\frac{\lambda}{500\ nm})^{-b_{Mie}})$ was fitted to the experimental data (Fig. 2B) using four fitting parameters: scaling factor a, describing the overall tissue absorption coefficients b, f_{Ray} describing the fraction of tissue absorption and Rayleigh scattering, and power factors b_{Mie} and n describing wavelength dependence for the tissue absorption and Mie scattering (Eq. (3) - 6). Uncertainties of fitting parameters are included. Scattering dominated the optical properties of the CLARITY- and CUBIC-treated samples, while for the iDISCO- and MASH-treated samples absorption contributes most. Both, Visikol- and ECi-treated samples, show a combination of absorption and scattering matching the macroscopic assessments.

Method	a	Absorption b	Rayleigh scattering f_{Ray}	Mie Scattering $(1\text{-}b\text{-}f_{Ray})$	b_{Mie}	n
CLARITY	0.0426±0.0004	0	0.8 ± 0.05	0.2 ± 0.05	0.6 ± 0.05	–
CUBIC	0.2846±0.003	0 ± 0.001	0 ± 0.003	1 ± 0.004	0.56±0.01	–
iDISCO	0.265±0.003	0.9 ± 0.007	0 ± 0.08	0.1 ± 0.15	1.3 ± 0.2	4.8 ± 0.03
MASH	0.5742±0.006	0.87±0.02	0.012±0.05	0.12±0.07	2.7 ± 0.1	3.5 ± 0.02
Visikol	0.47±0.005	0.27±0.005	0.36±0.02	0.36±0.03	0.5 ± 0.03	3.5 ± 0.1
ECi	0.73±0.007	0.29±0.01	0 ± 0.02	0.71±0.03	2.2 ± 0.02	3.5 ± 0.1
Control (Jacques, 2013)	4.01	0.1	0	0.9	3.1	3.5

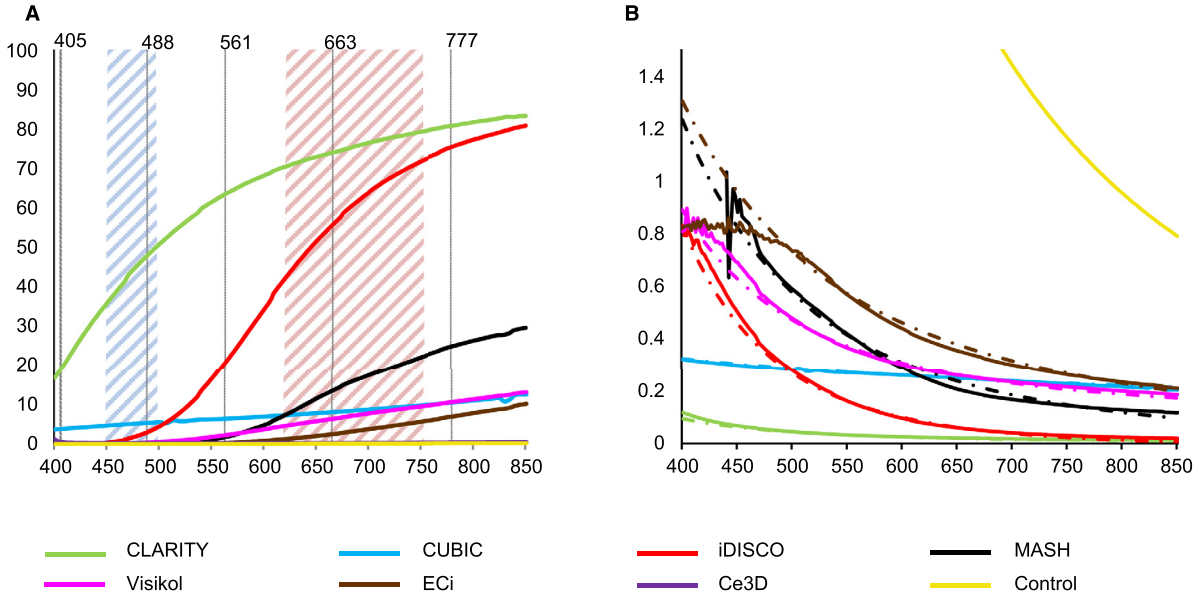

Fig. 2. Optical tissue properties achieved by seven tissue clearing techniques. (A) The amount of light transmission (TM) (in%) through the sample, at specific wavelengths (400 nm - 850 nm) is shown for seven cleared and one uncleared aged human brain tissue sample. All samples had an original thickness of 5 mm, except the MASH-treated sample with 2.5 mm thickness. For the MASH-treated sample the TM values were corrected (squared) to account for tissue thickness, which was a half of tissue thickness used for other methods. Blue hatched area indicates visible blue light (450 – 495 nm); red hatched area indicates visible red light (620 – 750 nm). Dotted lines indicate excitation wavelengths of commonly used secondary antibodies (Table 3) at 405 nm, 488 nm, 561 nm, 633 nm and 777 nm. Thereby, TM values at important wavelengths are displayed. Sufficient TM was defined as values ≥ 50%. Regardless of the degree of transparency, longer wavelengths led to higher TM values. Sufficient TM values were attained with the CLARITY- (green) and iDISCO-treated (red) samples. The MASH- (black), CUBIC- (blue), Visikol- (magenta) and ECi-treated (brown) tissue samples showed low TM values (≤ 20%). The Ce3D-treated (violet) sample showed no light TM and strong overlap with the measurement of the uncleared control tissue sample (yellow). (B) The effective absorption coefficient $\mu_{eff}(\lambda)$ (solid lines) was calculated for all samples using the modified Lambert Beer law (for details see Eq. (3)). For low scattering tissue the effective absorption coefficient is a sum of absorption and reduced scattering coefficients. The wavelength dependence of optical properties for all cleared samples except Ce3D can be very well theoretically described by the combination of Rayleigh and Mie scattering and absorption of melanin and lipofuscin (dashed lines) (for details see Eq. (6)). Lowest effective absorption coefficient at all wavelengths was achieved by the CLARITY-treated sample, which resulted in the averaged reduction of the effective absorption coefficient by a factor of 90.5 across wavelengths as compared with uncleared tissue (yellow). The parameters providing the best fit for $\mu_{eff}(\lambda)$ for each of the clearing methods are shown in Table 2.

sample, facilitated by underlying letters are shown in Fig. 1A. As reference (yellow), a *post mortem* fixed aged human brain tissue sample is shown to demonstrate the opacity of specimen before the clearing process. Overall clearing performance has been evaluated by the following criteria: letters legible, letters blurred, sharp sample edges, differences between gray matter (GM) and white matter (WM), tissue rigidity, difficulty to manipulate the tissue (later referred to as "tissue handling") and tissue deformation after clearing (Fig. 1A). All criteria were characterised as "xx": strongly/hard; "x": moderate; "-": easily/weak; "- -": not applicable and "n.e.": not evaluated. CLARITY- (green), CUBIC- (blue), iDISCO- (red) and MASH-treated (black) samples show legible underlying letters ("xx" or "x"). For CLARITY- und CUBIC-treated samples the letters appear blurred ("x"). Also, CLARITY-, CUBIC- and iDISCO-treated human brain samples show less sharp sample edges ("-") whereas MASH-treated sample shows sharp sample edges ("xx"). Strong differences between GM and WM are present in CLARITY-treated sample ("xx"). In contrast, Visikol- (magenta) and Ce3D-treated (violet) samples do not show legible letters ("- -") underneath either in GM or WM. Therefore, the blurriness cannot be evaluated ("n.e."). ECi-treated (brown) sample shows blurred letters ("x") becoming legible underneath GM ("x"). Hence, there are differences between GM and WM clearing when applying the ECi method to aged *post mortem* human brain tissue. Regarding

sharp sample edges, Visikol- and Ce3D-treated samples show less sharp sample edges ("-") compared to the ECi-treated sample ("x"). The tissue rigidity and difficulty to manipulate cleared tissue was altered by all protocols. The CLARITY- and CUBIC-treated samples showed low tissue rigidity ("-") and were hard to manipulate ("xx"). The iDISCO- and MASH-treated samples gain tissue rigidity ("xx"), enabling easy tissue handling ("-"). The latter applied to the Visikol-, ECi- and Ce3D-treated samples as well but with moderate effects ("x"). The overall tissue deformation (see Supplementary Information Fig. S1) during clearing differed between all clearing techniques. While the CLARITY- and CUBIC-treated samples deformed strongly ("xx"), the iDISCO-, MASH-, Visikol- and ECi-treated samples demonstrated low tissue deformations ("-"). The Ce3D-treated sample showed moderate tissue deformations ("x").

As an important efficiency criterion, the time needed to obtain macroscopic transparency was evaluated. Fig. 1B shows the time periods needed or reported in the literature to finish a clearing protocol. CLARITY- and CUBIC-treated brain tissue samples needed several months (≥ 5 months) to clear. iDISCO- and MASH-treated samples needed ≤ 1 month time to clear. The literature-based duration for high transparency with the Visikol, ECi or Ce3D method was also ≤ 1 month. However, 5 mm aged human tissue samples had not cleared after this time and remained in their respective clearing medium for 3 months. This prolonged incubation time did not add to the degree of transparency of any of the samples.

The change in sample volume was estimated. Fig. 1C shows the expansion or shrinkage of aged human brain tissue cleared with the investigated methods. When applying the CLARITY (green) method to aged *post mortem* human brain tissue, the tissue expands 146% in volume. On the opposite, the CUBIC-treated (blue) sample volume shrunk by 27%, the iDISCO-treated (red) sample shrunk by 24%, and the MASH-treated (black) sample shrunk by 4%. The Visikol-treated (magenta) sample shrunk by 9%, the ECi-treated (brown) human brain tissue sample shrunk by 16%, and the Ce3D-treated sample shrunk by 24% as well. The extent of this volume change seems to be independent of the overall level of macroscopic transparency reached.

In conclusion, we showed successful clearing of aged human brain tissue using the CLARITY and CUBIC clearing protocol, but they required several months clearing time and resulted in tissue volume change. Moreover, we demonstrated successful tissue clearing with the iDISCO and MASH clearing protocol. They required less than 1 month clearing time and led to tissue shrinkage. The ECi, Visikol and Ce3D clearing protocols did not clear human brain tissue in the proposed time and led to tissue shrinkage as well.

3.1.2. Optical properties

To support the macroscopic visual assessment of the clearing performance, the degree of transparency was quantified by measuring the amount of transmitted light travelling through the cleared aged human brain samples (Fig. 2A) with original thickness (before clearing) of 2.5 mm (MASH) or 5 mm (all other methods). An untreated sample was used as control. Generally, a sample was considered successfully cleared when it showed increased light TM and reached a maximum of ≥ 50% TM. This applies to the CLARITY- and iDISCO-treated samples. In addition, they showed an increase in transmitted light not only at higher but also at lower wavelengths. The CLARITY-treated sample showed 50% of transmitted light at wavelengths ≥ 496 nm and reached a maximum of 85% TM at 1000 nm. The iDISCO-treated sample showed 50% of transmitted light at 644 nm and a maximum of 86% TM at 1000 nm. The MASH-treated sample showed low TM values of 20% at 728 nm and a maximum of 37% transmitted light at 1000 nm. The CUBIC-, Visikol-, ECi- or Ce3D-treated aged human brain sample did not show sufficient transparency (≤ 20% of transmitted light even at the long wavelength of 940 nm). An untreated, *post mortem* fixed aged human brain tissue sample showed undetectable light TM at all wavelengths.

To further quantify the optical tissue properties, the effective absorption coefficient μ_{eff} for all tissue samples was calculated (Fig. 2B) and compared with the optical properties of uncleared brain tissue reported in the literature (Jacques, 2013). The effective absorption coefficient for a thin slab of low scattering tissue sample can be described as a sum of tissue absorption and reduced scattering coefficient. The later is determined by the combination of Rayleigh and Mie scattering. Fitting the wavelength dependence of μ_{eff}, the relative contribution of absorption and scattering could be determined. The wavelength dependence of effective absorption coefficient μ_{eff} was very well described by analytical expression (see Eq. (6)) for all samples except Ce3D, as can be seen in a well agreement between solid and dashed lines in Fig. 2B. The fitting parameters are presented in Table 2. The contribution of scattering and absorption to the overall tissue transparency is shown in Fig. S2 (Supplementary Information). The CLARITY-treated sample showed overall lowest effective absorption coefficient, with overall reduction by a factor of 90.5 as compared with literature values of uncleared brain tissue (Jacques, 2013). For CLARITY- and CUBIC-treated samples effective absorption was dominated by tissue scattering, while the iDISCO- and MASH-treated samples showed mostly light absorption with very low scattering contribution (Table 2, Supplementary Information Fig. S2). This describes the less steep dependence of optical properties on wavelengths for CLARITY- and CUBIC-treated samples. The Visikol- and ECi-treated samples showed a combination of tissue absorption and scattering in agreement with the macroscopic assessments.

In conclusion, TM measurements indicate that the CLARITY and iDISCO techniques generate cleared aged human brain tissue samples suitable for further processing and analysing.

3.1.3. Tissue clearing combined with immunohistochemistry

The wavelength-dependent analysis of light TM is of particular relevance for the microscopic analysis of immunofluorescence-treated human brain samples. Immunofluorescent processing visualizes cyto- and myeloarchitectonic structures due to bound fluorescent antibodies that emit light. This emission depends on antibody-specific excitation wavelengths. In Table 3, wavelength-specific TM values of all used clearing protocols are given. They correspond to excitation wavelengths of commonly used fluorescent-dye conjugated secondary antibodies and indicate which clearing protocol can be combined with which secondary antibodies in order to enable high light emission.

The wavelength-specific TM measurements differ significantly between the clearing techniques. For microscopic imaging, tissue absorption and scattering impact exciting as well as emitted light. Depending on the applied clearing protocol, light-scattering lipids seem to be dissolved or washed out differently. This results in different light absorption and scattering properties (Fig. 2, Table 2). Antibodies with high excitation wavelengths (≥ 561 nm), such as Cyanine 5 or 7, seem to be preferable. Vice-versa, labeling structures with antibodies excited with wavelengths < 561 nm is not recommended, especially when applying hydrophobic clearing protocols as iDISCO (Table 3). In conclusion, we recommend the use of secondary antibodies with longer excitation wavelengths for better light TM properties of cleared aged human brain tissue, in agreement with the known wavelength dependence of tissue absorption and scattering coefficients (Jacques, 2013).

3.1.4. Unifying macroscopic visual assessment and transmission measurements

Regarding the macroscopic findings (Fig. 1A), the optical properties achieved by seven tissue clearing techniques differed strongly between the techniques (Fig. 2). Generally, all macroscopically cleared samples, i.e. the CLARITY-, CUBIC-, iDISCO- and MASH-treated samples, show strong contrast between inside and outside the cleared tissue and are distinguishable from their background (Fig. 1A). Different degrees in blurriness of underlying letters indicate varying light scattering. Different contrasts between a cleared sample and its background indicate varying intensities of transmitted and backscattered light. However, the low TM values of the CUBIC- and MASH-treated sample (Fig. 2A) do not match these macroscopic findings.

Table 3
TM values [%] for seven clearing techniques given at wavelengths corresponding to excitation wavelengths of commonly used secondary antibodies. A reference wavelength is given for each range of excitation wavelength. Highlighted values show sufficient TM values (≥ 50%) as indication for useful wavelengths when applying fluorescent secondary antibodies to cleared aged human brain tissue.

	DAPI, Hoechst 3335 (350–465 nm)	Alexa 488, FITC, Cy2, GFP (480–520 nm)	DiI, Cy3 (550–565 nm)	TO-PRO3, Cy5 (640–665 nm)	Cy7 (750–780 nm)
Reference λ	**405nm**	**488nm**	**561nm**	**663nm**	**777nm**
CLARITY	19%	48%	63%	74%	81%
CUBIC	0%	5%	6%	8%	10%
iDISCO	0%	3%	20%	56%	75%
MASH	0%	0%	2%	13%	25%
ECi	0%	0%	0%	2%	7%
Visikol	0%	0%	2%	6%	11%
Ce3D	0%	0%	0%	0%	0%
Control	0%	0%	0%	0%	0%

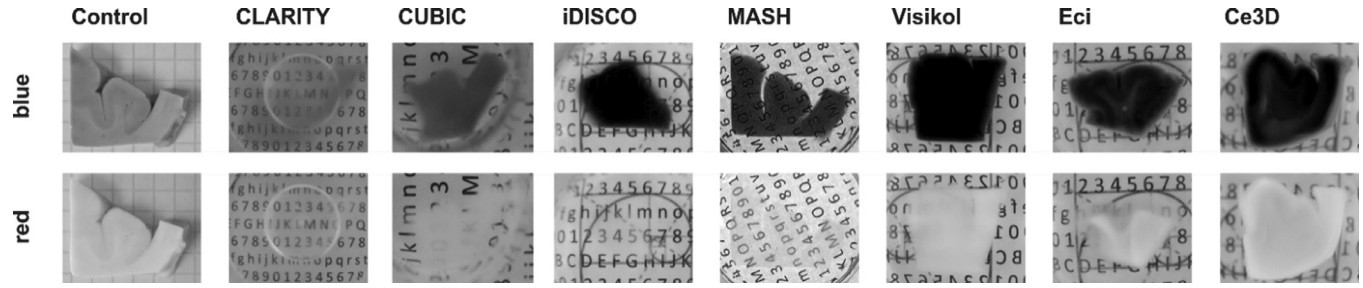

Fig. 3. Extracting blue and red channel values from gray-scaled images of macroscopic findings. Top row shows blue color channel; bottom row shows red color channel extracted from RGB photographs of CLARITY-, CUBIC-, iDISCO-, MASH-, Visikol-, ECi-, and Ce3D- treated human brain sample as well as control sample (all *Gyrus cinguli* with/without *Corpus callosum*, sample 1a-e & 2a,b). Differences in contrast between cleared aged human brain tissue and its background indicate a correlation of light TM to applied wavelength. The contrast between cleared sample and background is higher in the blue channel than in the red channel in line with higher light TM at longer wavelengths. Note, that the tissue block used for MASH technique had lower thickness as compared to the blocks used for the other techniques (2.5 mm for MASH as compared to 5 mm for other methods, see Table 1). Therefore, in red channel it appears comparably transparent to sample cleared with iDISCO, despite of much higher effective absorption coefficient for the MASH-treated sample.

Therefore, we took a closer look at individual color channels of macroscopic images to help reconcile both results. We extracted red and blue color channels, indicated as hatched areas in Fig. 2, from RGB tissue photographs to evaluate effective light intensities (Fig. 3). They show how blue and red light reflects from and transmits through the sample. The most pronounced differences between sample and background are visible in the blue channel (Fig. 3, top row). The CLARITY- and CUBIC-treated samples show weaker contrast than the iDISCO-, MASH-, Visikol-, ECi-, and Ce3D-treated samples. Interestingly, in the CLARITY-treated sample, WM areas show higher contrast against the background compared to GM areas. In the red channel, contrasts between sample and background are drastically reduced or reversed. The CLARITY- and iDISCO- treated samples could not be identified macroscopically as light seems to be neither scattered nor absorbed. Contrasts between CUBIC- and MASH-treated samples and their background were weak as well. For Visikol-, ECi- and Ce3D-treated samples, the contrast was higher inside the sample compared to the background. The proportion of reflected light strongly increased as almost no light passes through the sample.

These findings from the extracted color channels indicate that the CLARITY- and CUBIC-treated samples show higher light TM for short wavelengths (blue part of the spectrum) compared to the iDISCO- and MASH-treated samples. This difference seems to decrease at longer wavelengths (red part of the spectrum) as light transmits well through CLARITY-, CUBIC-, iDISCO- and MASH-treated human brain samples (Fig. 3, bottom row). Nevertheless, CLARITY outperforms all other methods at all wavelengths and the CUBIC-treated sample shows less light TM at longer wavelengths compared to the iDISCO and MASH-treated sample. This aligns with the less steep increase in transmitted light (between 340 – 520 nm) for iDISCO- and MASH-treated samples compared to the CLARITY-treated sample (Fig. 2). Generally, the higher the contrast between background and tissue, the longer the wavelength needs to be in order to pass through it. In conclusion, macroscopic visual assessment and measurements of optical properties congruently show that sufficient light TM is wavelength-dependent for it to transmit cleared human brain tissue sample.

3.2. Microscopic imaging of cleared aged human brain tissue

3.2.1. Wavelength-specific imaging of four differently cleared human brain samples

Macroscopic visual assessments and measurements of optical properties concluded that three techniques (CLARITY, iDISCO, MASH) successfully cleared aged human brain tissue. Due to sufficient macroscopic findings, we included a CUBIC-treated sample in microscopic imaging of cleared human brain tissue. All four cleared and fluorescently labeled samples underwent microscopic imaging (Fig. 4). Depending on the used antibody combination, different excitation wavelengths detect different structures. Images in B1-4 show autofluorescent (AF) structures excited at 405 nm. C1 and C2 show β-lll-tubulin whereas C3 and C4 show AF; excited at 488 nm. D1, D2 and D4 show labeled myelin (MBP), D3 shows AF; excited at 561 nm. E1, E3 show structures labeled for myelin (PLP), E2 and E4 show AF, excited at 633 nm. There is a strong overlap between immunohistochemically labeled and AF structures. Hence, Fig. 4 gives rise to considering AF structures as valuable information when dealing with immunohistochemically processed aged *post mortem* human brain tissue.

For CLARITY- (B1 – E1) and CUBIC-treated (B2 – E2) samples, light emission decreased with larger, lower energy wavelengths as overall light intensity of microscopic images fades along column 1 and 2. This is not true for the iDISCO- (B3 - E3) and MASH-treated (B4 - E4) sample. The iDISCO-treated sample emitted strongest at 633 nm (E3), the MASH-treated sample at 561 nm (D4). Interestingly, no light emission was detected when the MASH-treated sample was excited at 405 nm (B4). Microscopic imaging parameters (i.e. imaging depth at 300 µm beneath

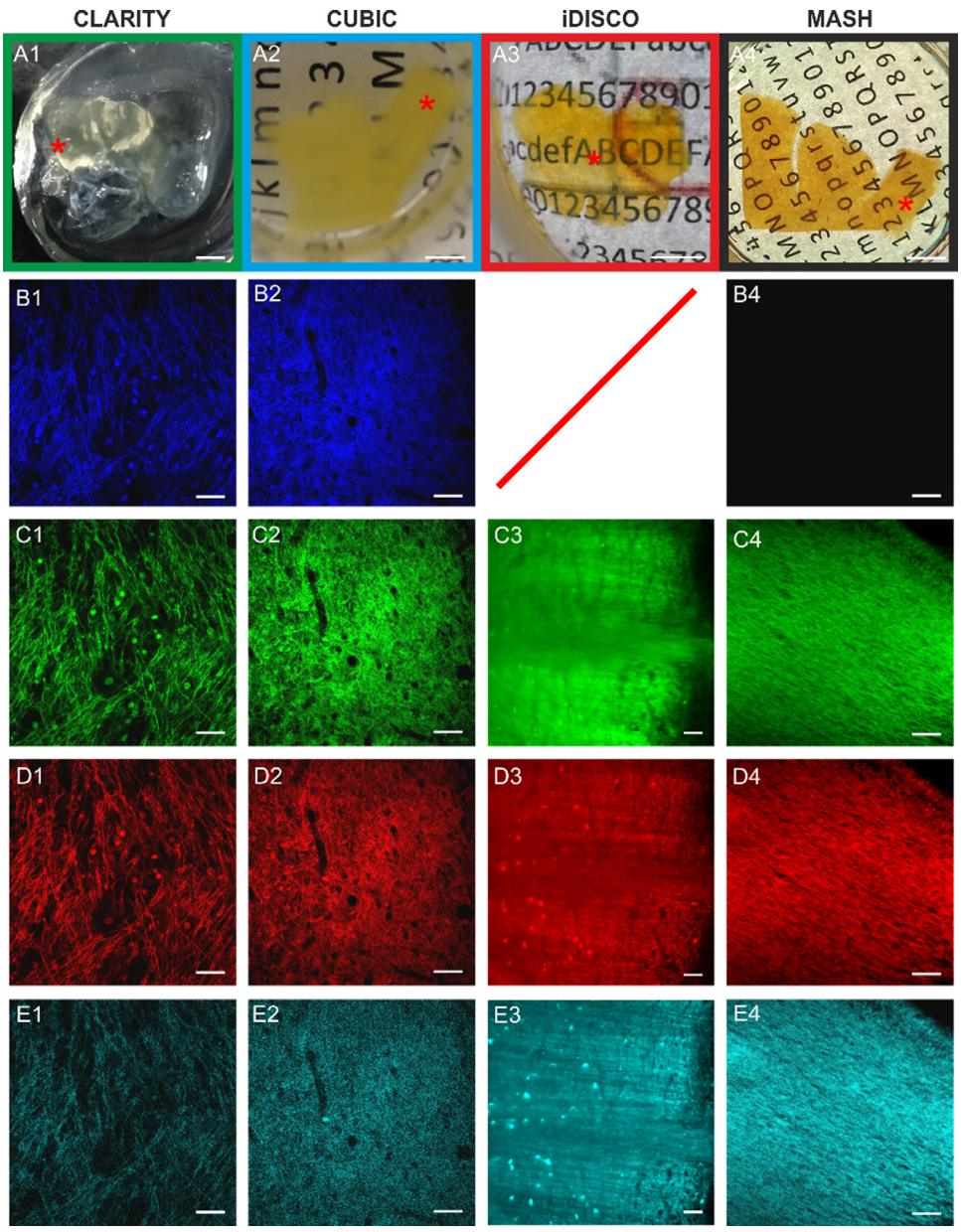

Fig. 4. Wavelength-specific microscopic imaging of four cleared human brain samples in WM regions. All samples have been cleared individually using either the CLARITY (A1 – E1: *Chiasma opticum*, sample 3), CUBIC (A2 – E2: *Gyrus cinguli* with *Corpus callosum*, sample 1b), iDISCO (A3 – E3: *Medulla oblongata*, sample 4) or MASH (A4 – E4: *Gyrus cinguli* with *Corpus callosum,* sample 1c) technique and immunohistochemically processed. First row (A) shows macroscopic view of samples after clearing. Scale bar = 1 cm. Asterisk indicates field of view (FOV) in B – E. Second row (B) shows samples excited at 405 nm; third row (C) shows samples excited at 488 nm; fourth row (D) shows samples excited at 561 nm; fifth row (E) shows samples excited at 633 nm. Scale bar (B – E) = 50 µm. The CLARITY-, CUBIC-, and MASH-treated samples were imaged with the Zeiss laser scanning microscope (LSM) 880. The iDISCO-treated sample was imaged with the Miltenyi Biotec Ultramicroscope II (UM II). The UM II is not equipped with a UV laser, hence the microscopic image at 405 nm cannot be provided. All antibody-specific wavelengths showed equal light emission. Images in (B) show autofluorescent structures (AF). C1 and C2 show tubulin (β-III-Tub) whereas C3 and C4 show AF. D1, D2 and D4 show labeled myelin basic protein (MBP); D3 shows AF. E1 and E3 show labeled proteolipid protein (PLP), E2 and E4 show AF.

the tissue surface and laser settings) were kept consistent throughout the imaging process. In conclusion, microscopic imaging of four differently cleared aged human brain samples with two different microscopic setups is feasible.

3.2.2. Depth of microscopic imaging of four differently cleared aged human brain samples

The penetration depth of light is essential for imaging cleared aged human brain tissue. At the same time, the penetration depth of antibodies needs to be taken into account when clearing is combined with immunohistochemistry. Macroscopic visual assessments and measurements of optical properties showed transparency and sufficient light TM for CLARITY (A: *Chiasma opticum*), iDISCO (C: *Medulla oblongata*) and MASH (D: *Gyrus cinguli* with *Corpus callosum*) clearing techniques. Due to promising macroscopic findings, we included a CUBIC-treated sample (B: *Gyrus cinguli* with *Corpus callosum*) in this evaluation. All samples were excited at 561 nm; (A), (B) and (C) show Cy3-conjugated rat-anti-MBP whereas (D) shows Red Fluorescent Myelin Stain (FluoroMyelin^{TM}). Although, due to experimental limitations (i.e. unsuitable DBE (iDISCO) for Zeiss LSM 880) quantitative interpretations of this results are challenging, its practical relevance becomes apparent. The range of microscopic mapping varies between the different clearing techniques. The CLARITY- (A) and iDISCO-treated samples (C) could be imaged along their entire z-axis (2500 µm imaging depth) with (C) showing the sample's borders at both ends. The CUBIC- (B) and MASH-treated samples (D) show limited light penetration along their z-axis. In (B), light emission fades out after 1000 µm whereas the fluorescent signal in (D) is lost before 500 µm. Nonetheless, Fig. 5 shows that macroscopically transparent samples do not emit light consistently when imaged with a confocal laser scanning microscope (LSM) nor a light sheet microscope (UM II).

3.2.3. Comparison of three microscopic imaging setups suited for imaging large-scale specimen

Fig. 6 shows a piece of aged human cerebral WM (*Corona radiata*, sample 4a) imaged with three different microscopic setups. This piece was cleared with the CLARITY technique and immunohistochemically processed to show myelin (anti-PLP; A) and astrocytes (anti-GFAP; B).

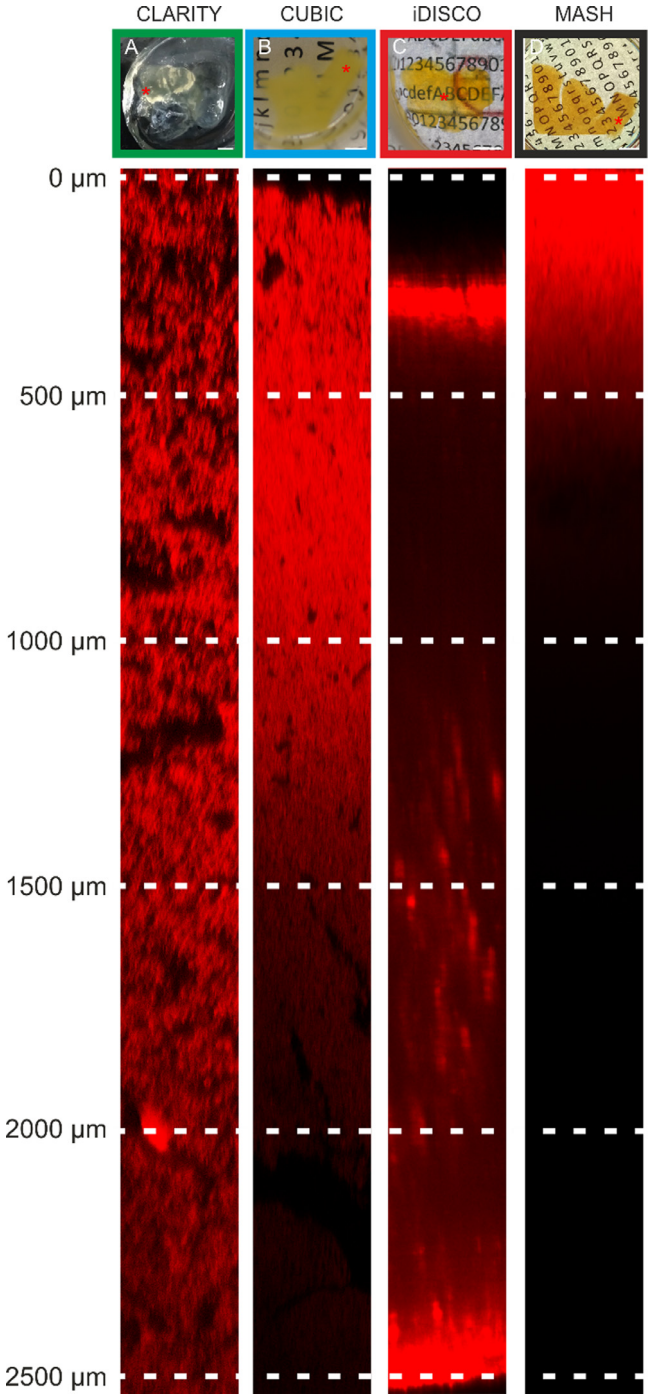

Fig. 5. Comparing microscopic imaging depths of four successful tissue clearing techniques. CLARITY- (A: *Chiasma opticum,* sample 3), CUBIC- (B: *Gyrus cinguli* with Corpus callosum, sample 1b), iDISCO- (C: *Medulla oblongata,* sample 4b) and MASH-treated (D: *Gyrus cinguli* with *Corpus callosum*, sample 1c) samples were imaged at 561 nm along their z-axis (reconstructed z-line scan) to evaluate antibody and light penetration in cleared aged human brain tissue. Range of mapping was set to 2500 µm along z-axis. 500 µm steps are indicated by dashed line from 0 µm to 2500 µm. (A), (B) and (C) show Cy3-conjugated rat-anti-MBP whereas (D) shows Red Fluorescent Myelin Stain (FluoroMyelin™). (A), (B) and (D) were imaged with the Zeiss LSM 880, (C) was imaged with the Miltenyi Biotec UM ll. Note, apart from different efficiency of antibody penetration, several other factors (e.g. optical properties, geometry of the microscope, etc.) contribute to observed differences in imaging depth between methods. Thus, presented depth profiles could not be used for quantitative method comparison, but are shown for illustrative purpose to demonstrate strong variations in imaging depth between methods. (A) and (C) show consistent light emission, with (A) showing a decreasing signal after 1500 µm and (C) showing an intensified signal at sample borders above 500 µm and at 2500 µm. (B) and (D) show a fading signal above 1500 µm and 500 µm, respectively.

The Zeiss LSM 880 with a 20x Clr objective (numerical aperture (NA) 1.0, working distance (WD) 5.6 mm) was used for the images in column 1, the Miltenyi BioTec UM ll with a 12x immersion objective (NA 0.53, WD 10 mm) for column 2, and the 3i Marianas LightSheet microscope with two 20x immersion objectives (NA 0.5, WD 3.5) for column 3. Images taken with the LSM 880, which achieved the highest resolution, show myelinated structures (A1) and astrocytes (B1) when the cleared aged human brain sample is excited at 488 nm and 561 nm, respectively. Both structures appear parallel and intertwined, with astrocytes filling the spaces between myelinated structures (C1). When the sample is imaged with the UM ll, a bigger field of view (FOV) with lower resolution can be obtained. This results in less detailed images, which may appear blurry depending on sample movement and the chosen illumination plane (A2 – C2). Nevertheless, both labelled structures are separable with crossing and parallel myelin structures (A2/C2) and adjacent astrocytes (B2). Eventually, the sample was imaged with the 3i Marianas LightSheet, using only one light path. Generally, there are two perpendicular objectives alternating between excitation and detection. This creates two focal planes with isotropic resolution. Compared to the LSM 880 and UM ll, the sample is imaged in a 45° angle to its surface and scanned along this optical plane (Fig. 6D). This leads to microscopic images (column 3) showing hydrogel as well as cleared and uncleared parts of the sample. Different AF properties of myelin (A3) compared to astrocytes (B3) stand out. While a frame-filling signal of myelin and AF (A3) can be detected in the uncleared area, the sample shows a more specific GFAP signal within the cleared areas (B3) when excited at 561 nm (see Fig.6D). Large amounts of AF make it difficult to isolate PLP signal, especially when merging the signal of both channels (C3). Here, overlapping structures remain absent. Also, it is harder to identify the sample or fiber orientation due to the uncommon detection plane. Compared to the LSM 880 (column 1) and the UM ll (column 2), no crossing or parallel pattern of myelinated structures can be recognized (A3/C3) when the sample was imaged with the 3i Marianas LightSheet.

4. Discussion

In this study, seven tissue clearing techniques were tested on mm-sized aged *post mortem* human brain tissue samples to determine the most efficient one. Efficiency is defined as rendering a tissue sample transparent, preserving the ability for immunohistochemical staining of the tissue before or after clearing, and short experimental processes. Thereby, consistent antibody and light penetration during microscopic imaging needs to be accomplished. The CLARITY, CUBIC, iDISCO, and MASH techniques were able to clear aged human brain tissue, whereas the ECi, Visikol and Ce3D method were not (Fig. 1). During tissue clearing, optical properties are altered and transparency is increased by reducing light absorption or scattering (Fig. 2, Table 2, Supplementary Information Fig. S2). Microscopic imaging revealed that the CLARITY and iDISCO techniques are most suitable for clearing aged human brain tissue (Fig. 4, Fig. 5). Here, fluorescent antibodies as well as light penetrated sufficiently deep into the tissue (Fig. 5). Moreover, this study examined three different microscopic setups to identify the benefits and downfalls of each setup for imaging large-scale specimen (Fig. 6). In summary, the results showed that the most suitable and efficient clearing approaches are to combine the CLARITY tissue clearing technique with Zeiss LSM 880 imaging or to combine the iDISCO tissue clearing with Miltenyi Biotec UM ll imaging.

Tissue transparency

Tissue transparency is reached when light scattering molecules like lipids are removed (Dodt et al., 2007) while light absorption is reduced (Kerker, 1969; Johnsen and Widder, 1999). Pigments like heme or melanin hinder this reduction as they are endogenous structures absorbing light (Monici, 2005). These pigments as well as lipids accumulate over time (lipofuscin) and contribute to colorization of the human brain (Goyal, 1982; Morawski et al., 2004). By absorbing light, overall light TM of the tissue is weakened and AF is increased (Fig. 4, Fig. 5).

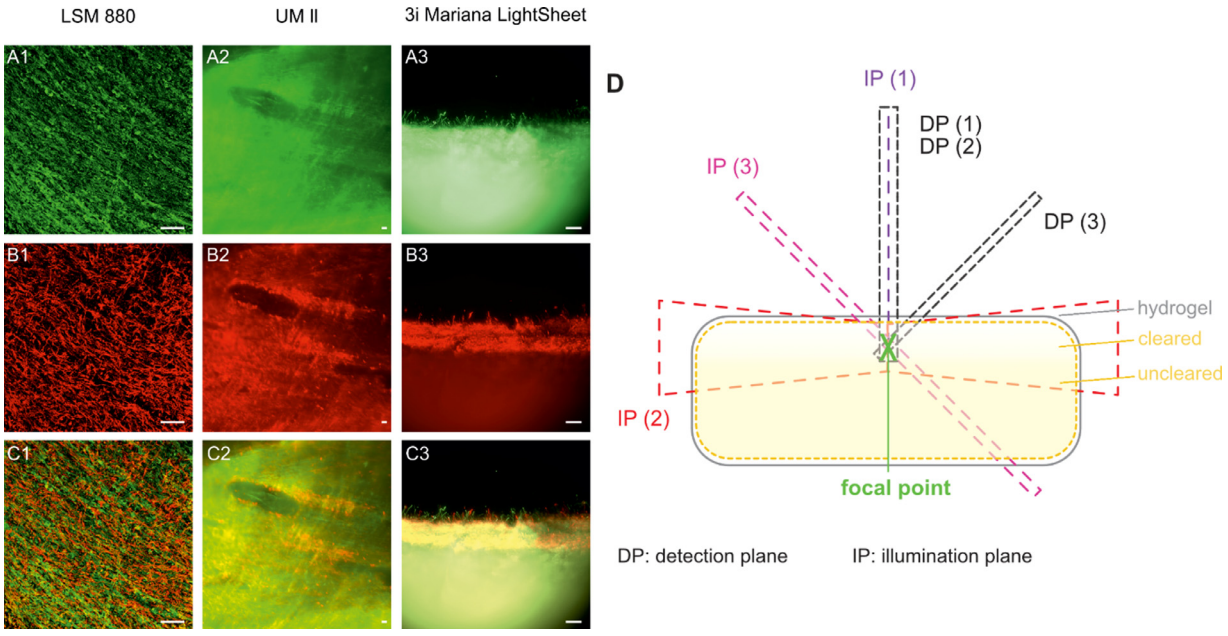

Fig. 6. Comparing three microscopic setups used for large-scale imaging. (A-C) An aged *post mortem* human WM piece (*Corona radiata,* sample 4a) was CLARITY-treated, immunohistochemically processed and imaged with three different microscopic setups. Column 1 shows the sample imaged with the Zeiss LSM 880, column 2 shows the sample imaged with the Miltenyi BioTec UM ll and column 3 shows the sample illuminated with one imaging path of the 3i Marianas LightSheet microscope. First row (A) shows myelin (anti-PLP), excited at 488 nm. Second row (B) shows astrocytes (anti-GFAP), excited at 561 nm. Third row (C) shows merged images of excitation at 488 nm and 561 nm to show overlapping structures. Columns 1 and 2 show the sample from z-perspective. Column 3 shows the sample illuminated and detected in a plane at an angle of 45° with respect to the tissue surface, displaying cleared (upper image part) and uncleared areas (lower image part) within the sample. Scale bar = 50 µm. (D) The schematic drawing illustrates the illumination (IP) and detection plane (DP) of the three microscopic setups used for imaging the CLARITY-treated sample (300 µm thickness, x = focal point). The three layers of the sample are indicated as hydrogel, cleared and uncleared. Focal point is dissimilar to imaged area. FOV was within cleared part, except column 3 where cleared and uncleared areas were detected. The LSM 880 emits a confocal laser beam into the sample, 90° to the tissue surface but congruent to the DP. The UM ll emits up to three light sheets (≥ 4 µm) into the sample, perpendicular to the sample surface and the DP. The 3i Marianas LightSheet microscope emits a light sheet perpendicular to the DP but creates an optical plane of 45° to the tissue surface.

Therefore, decolorization or bleaching steps can be advantageous when clearing aged human brain tissue (Renier et al., 2014). This is true for the iDISCO and MASH protocols, where absorption dominates light absorption in the cleared tissue (Table 2) and may be even enhanced as compared to uncleared tissue due to the oxidation of tissue components. The reduction of light absorption within tissue blocks also leads to higher levels of light TM (Weissleder, 2001; Tuchin, 2015). Due to different refraction and scattering properties within a cleared sample, light TM is different for each clearing approach. Next to iDISCO- and MASH-cleared samples, CLARITY- and CUBIC-cleared samples achieve high levels of TM (Fig. 2), although no separate decolorization is performed during the clearing procedure (Chung et al., 2013; Susaki et al., 2015). Light's physical properties are modulated by the interaction of clearing medium and aged *post mortem* human brain tissue sample.

The combination of exo- and endogenous fluorescence

After attaining transparency, the application of immunohistochemistry remains crucial. Higher TM values observed at higher wavelengths (Fig. 2) suggest that secondary antibodies with longer excitation wavelength may be preferable (Table 3). The nearly exponential increase of light TM (Fig. 2) describes the well-known dependency of wavelength and light scattering in biological tissue (Jacques, 2013). Additionally, microscopically detectable fluorescence needs to be differentiated between induced fluorescence (by exogenous fluorophores, i.e. cyanine 2, 3, 5) and AF (endogenous fluorophores). Taking AF into account, which is strongest at short wavelengths (Monici 2005), the range of usable light emission when working with laser microscopes expands (Fig. 3). In fluorescence microscopy, AF is regarded as complicating identification of cellular structures. It arises from endogenous fluorophores that are stored mainly in mitochondria, lysosomes and blood vessels (Monici, 2005). In human brain tissue, especially lipofuscin, an intralysosomal cluster of proteins and lipid, and collagen, as part of arteries, are responsible for emitting fluorescence due to high quantum yields (Morawski et al., 2004; Monici, 2005). Quantum yields of fluorophores (endo- and exogenous) are defined as the number of photons emitted to the number of photons absorbed by a system (Lakowicz, 1983a). Fluorophores with shorter excitation wavelength have smaller quantum yields than fluorophores with longer excitation wavelength. This leads to an increased probability of spontaneous light emission (Monici, 2005) and thus to higher AF, particularly at shorter excitation wavelengths. Hence, endogenous fluorophores combined with spontaneous light emission of exogenous fluorophores lead to AF. However, when focusing on the myeloarchitecture of cleared human brain tissue working with AF and quantifying it may be of interest. Myelin sheaths of axons are composed of lipids and proteins, prone to emitting AF. In turn, taking advantage of this effect and imaging AF of myelinated nerve fibers could be useful to study axonal distribution and structure tensor aspects. Although AF can only partially substitute flexible and specific immunohistochemical processing due to its low specificity, the advantages of AF signals in experimental procedures have been long overt (Buhl and Schlote, 1987). Especially the combination of tissue clearing and AF has found a broader audience in diagnosis and other pathological examinations recently (Sabdyusheva Litschauer et al., 2020; Hahn et al., 2020).

Antibody and light penetration

Due to individual quantum efficiency of antibodies (Monici, 2005) combined with their limitations in reliability, antibody-specific fluorescence contributes differently to detected light (Anger et al., 2006) of a cleared aged human brain sample. Also, different inter-methodological scattering and absorption properties (Fig. 1- 4) lead to unpredictable correlations between cleared tissue and fluorescent antibodies. Hence,

it remains uncertain whether fluorescent signals vary due to different antibody or light penetration depths (Fig. 5). Due to individual experimental prerequisites when clearing aged human brain tissue with different methods, it is often difficult to quantify the contribution of single factors such as optical properties or antibody penetration to the overall imaging depth. However, these very evident differences when investigating tissue clearing and its practical relevance gives reason to extent this finding in future studies.

It is most likely that fluorescent signal is lost due to a combination of lack of antibody or light penetration (Ando et al., 2014), quenching (Lakowicz, 1983b), bleaching, and other cleared-tissue specific light TM features.

Different refractive index matching solutions

Investigating seven different clearing techniques brought up many challenges in each of the techniques. Although processing steps can be identical (Tian et al., 2020), there are differing steps within each technique as well. The biggest difference lies in the refractive index matching solution (RIMS) of each clearing technique and with it a medium-specific RI (1.48 - 1.56). Hydrophobic techniques aim for higher RI, with RI > 1.5, whereas hydrophilic techniques aim for lower RI, with RI < 1.5. Considering the RI of intact biological tissue of 1.47 – 1.51 (Jacques, 2013; Costantini et al., 2019) hydrophilic methods seem to be more favorable (RI < 1.5) with the approach of homogenizing the native RI of biological tissue instead of increasing it. The RIMS TDE was used twice in this study (CLARITY and MASH protocols) due to its low impact on subcellular alterations during clearing and its flexible RI (Hildebrand et al., 2019). By diluting TDE its RI can be adjusted from 1.33 to 1.52. Both protocols used similar concentration of TDE (62% vs. 63%) as this leads to highest transparency in aged human brain tissue while having smallest microstructural impact, i.e. shrinkage or expansion of tissue (Costantini et al., 2015). In this study, the CLARITY-cleared aged human brain tissue expanded approx. 146% in size compared to its original sample size (Fig. 1). Nevertheless, decreasing the TDE concentration to 47% as postulated by Costantini et al. in 2015 might aggravate tissue swelling. Although Morawski et al., 2018 showed human brain tissue shrinking again using 47% TDE eventually, previous experiments to this study (not shown here) demonstrated that 47% TDE is not suitable for clearing mesoscopic-sized aged human brain tissue blocks. Due to enlarged tissue surface, 26 × 18 mm^2 (x-y-direction of tissue sample), too much water is introduced into the sample that may destabilize its molecular structure, strongly aggravating its integrity and handling.

Tissue volume change

It remains elusive whether this tissue expansion of the CLARITY technique may be advantageous (Cho et al., 2018; Bürgers et al., 2019). Firstly, light penetration may benefit from this expansion due to reduced tissue scattering and absorption properties. However, pronounced differences in light penetration properties of the CLARITY-, CUBIC-, iDISCO-, and MASH-cleared sample occurred regardless of tissue expansion or shrinkage (Fig. 5).

Secondly, variable molecular processes happen between human brain tissue and optical clearing medium, influencing diffusivity, macromolecule content, and preservation of induced antibodies (Costantini et al., 2019). Hence, increasing the integrity of biological tissue and stabilizing its microstructure regardless of the used clearing technique could be another suitable approach. Similar to pretreating samples with hydrogel, the SHIELD approach enhances the cross-linkage of biomolecules internally and externally by introducing a flexible polyepoxide into the sample. Moreover, it improves fixation of biophysical properties by 50 - 400% compared to PFA or GA (Park et al., 2018). However, further biochemical and biophysical investigations are needed to elucidate the molecular processes responsible for difference in light absorption and scattering between techniques (Kim et al., 2018) and their influence on light and antibody penetration.

Thirdly, decreasing the dense nature of human central nervous tissue can be advantageous, e.g. when studying human myeloarchitecture (Hellwig, 1993; Murray et al., 2015; Morawski et al., 2018). Although it has not been quantified whether the swelling occurs homogenously throughout human neuronal microstructure, microscopic imaging suggests that the overall tissue structure has loosened up during the CLARITY clearing process (Fig. 4 A1 - E1). By clearing aged human brain tissue with the CLARITY technique, the axonal fiber distribution appears spaced out (Fig. 4 D1). In 2014, Ando et al. noted, that regardless of swelling during clearing, the continuity of axons and morphological structure stays intact. Hence, identifying and tracking individual fiber pathways may become feasible. This poses an interesting problem for (semi-)automated labeling and analysis tools. However, the task of fiber tracking in microscopically resolved images of cleared aged human brain tissue has yet to be mastered by deep learning and machine learning approaches (Helmstaedter and Mitra, 2012; Helmstaedter, 2013; Morawski et al., 2018) and remains extremely difficult.

Further differences between methods

The CLARITY method comes with disadvantages as well. Applying it to aged human brain tissue results in a gel-like sample that is difficult to handle and prone to moving (Fig. 1, Supplementary Information Fig. S1). This can be reduced by embedding it in TDE-agarose before imaging. The time issue needed for clearing can be overcome by improving fixation, washing, and antibody penetration by perfusing the human brain (Hildebrand et al., 2020; Zhao et al., 2019). This way, incubation times can be shortened and antibody penetration is accelerated. Additionally, eliminating the hydrogel step from the CLARITY protocol might save up to two weeks (Liu et al., 2017).

Generally, all technical aspects (e.g. hydrogel preparation, electrophoretic chamber acquisition) of the CLARITY method are time and cost consuming. Here, the iDISCO, MASH, and ECi protocols are more efficient. Their material costs are lower and, if successful, the processing duration is short compared to the CLARITY technique.

Although, the Visikol (commercial clearing kit) and Ce3D technique claim to be quickly applied and to clear tissue fast, they can be less affordable and more complex to perform as well.

The handling of iDISCO-treated samples is more manageable compared to CLARITY-or CUBIC-treated samples due to shrinking and stiffening of the human brain tissue. This is also true for the MASH-, Visikol-, ECi-, and Ce3D-treated samples. However, these protocols, except MASH, did not clear aged human brain tissue, making microscopic imaging impossible.

Regardless, the disadvantage of longer clearing periods when using the CLARITY technique is outweighed by 100x reduced tissue absorption and scattering compared to uncleared biological tissue. This is a reduction by factor 10 compared to the other clearing techniques (Table 2). Moreover, the pace of the iDISCO technique is diminished by the used imaging medium (DBE), which is less versatile and riskier due to its aggressivness (Renier et al., 2014).

Microscopic setups tailored to clearing methods

Microscopic evaluation of clearing efficiency of different techniques remains challenging as many parameters influence the imaging process. Facing an increasing number of immersion objectives with various RI and large working distances (WD) for each microscope (for a detailed overview, refer to the comparison of microscopy setups, Table S2 in the Supplementary Information), microscopy requirements need to be considered in tissue clearing. A suitable objective has to achieve the targeted resolution and meet the demands of the sample and the RIMS.

Besides different magnifications and NA, a suitable objective has to allow for the RI of the immersion medium needed to achieve optimal microscopy results. The objectives used in this study have either fixed RI (Zeiss LSM 880, 3i Marianas LightSheet) or adjustable RI (Miltenyi Biotec UM ll). For instance, due to RI restrictions, the 20x Olympus objectives (RI = 1.33) of the 3i Marianas LightSheet microscope are neither well-suited for imaging CLARITY-cleared samples in 63% TDE (RI = 1.45) nor iDISCO-cleared samples in DBE (RI = 1.56). It is possible to circumvent these limitations using alternative objectives, such as two 16.7x Special Optics clearing objectives (RI = 1.45). However, using these alternative objectives entails further computational process-

ing and complicates the experimental procedure (for more details, see Supplementary Information).

Furthermore, an objective may constrain the types of usable immersion media. For instance, Olympus and Zeiss recommend against organic solvents as immersion media, hence disallowing iDISCO-treated samples immersed in DBE.

Notably both, imaging CLARITY-cleared samples with the Zeiss LSM 880 and imaging iDISCO-cleared samples with the Miltenyi Biotec UM ll achieved the imaging goals of this study. The highest-resolution 3D images were acquired with the 20x objective at the Zeiss LSM 880. Nevertheless, there was a tradeoff between high resolution ($\geq$ 0.32 μm) and low imaging speed (27 fps). On the other hand, the UM ll generated large-scale images of cleared samples at high imaging speed (100 fps). This microscope was able to image all samples of this study in their respective RIMS, as both objectives (2x/12x) have a RI correction ring and are organic solvent safe. The drawback of the UM ll are its lower resolution due to the smaller NA of the objectives and restricted light sheet thickness ($\geq$ 4 μm) (Supplementary Information Table S2).

Mismatched RI between objectives (e.g. Zeiss Clr Plan-Apochromat objective with RI = 1.38) and RIMS (e.g. ECi with RI = 1.56) during imaging can lead to blurred and poorly resolved images, impeding overall experimental outcomes. Moreover, handling and processing 3D microscopic data is pivotal in imaging cleared tissue (Richardson and Lichtman, 2015; Tian et al., 2020). Working with TB-sized 3D data sets, which often occur in the presented approaches, leads to special soft- and hardware requirements (Ueda et al., 2020).

Photobleaching

The degree of photobleaching during image acquisition is another factor to be considered when comparing different microscopes. Photobleaching is determined by the product of total light power delivered per sample volume and overall imaging time. Simple estimation provided in the Supplementary information demonstrate that light sheet microscopy is a less phototoxic imaging method causing much less photobleaching as compared to confocal laser scanning microscopy.

Potential of 3D histology in cleared human brain tissue

Three-dimensional histology, e.g. applying tissue clearing, bridges standard histological thin-sectioning (2D) and non-invasive imaging techniques like MRI, positron emission transmission (PET) or computed tomography (CT) (Morawski et al., 2018). Histological sectioning generates 2D microscopic images with (sub)cellular resolution of $\geq$ 0.24 μm. Non-invasive imaging techniques generate 3D images of anatomical structures within minutes. In exchange, resolution is 1000x lower (> 220 μm) and information is lost (Gómez-Gaviro et al., 2020). It is possible to reconstruct 3D anatomical structures from 2D histological sections but the amount of time and energy needed is immense (Helmstaedter et al., 2011; Helmstaedter, 2013; Amunts et al., 2013; Abe et al., 2017). The goal is to fill this gap by introducing a wide-scale (mm-sized) multimodal imaging of microscopically resolved ($\leq$ 10 μm) tissue blocks. This can be achieved by using tissue clearing techniques and light sheet microscopy. Next, it becomes desirable to execute a pipeline including all scales (2D and 3D (tissue clearing and MRI)) in one sample. This way, resolution and sample size can be increased stepwise to create microstructure-informed MRI data and enable its histological validation.

Developments in tissue clearing that further-process cleared tissue samples are adding to this idea of a whole-scale pipeline. In 2020, Zhanmu et al., al. performed a combination of tissue clearing and paraffin-embedding of cleared rodent and macaque brain tissue. Another approach was taken by Sabdyusheva Litschauer et al. (2020), who did a 3D reconstruction of thin-sectioned human tumor tissue after clearing it with pathoDISCO, fully reversing it and executing histological processing (haematoxylin-eosin stain). Thereby, another level of histological evaluation can be added.

Outlook

Although transparency of aged human brain tissue is reached with the CLARITY and iDISCO methods, the question remains whether more suitable clearing techniques arise and improve the clearing process for (aged) human brain. Further promising methods include OPTIClear (Lai et al., 2018) and hFRUIT (Hildebrand et al., 2020). On the one hand, OPTIClear proposes to clear native and aged human brain tissue with TDE and iohexol for homogenizing RI of hydrophilic and lipophilic cell compartments, respectively. However, after unsuccessfully applying the Ce3D method which uses histodenz instead of iohexol as a non-ionic density gradient medium, it seems unlikely to achieve transparency with OPTIClear in aged human brain tissue. On the other hand hFRUIT, is an improved version of the FRUIT method (Hou et al., 2015) where DiI-stained *post mortem* human brain tissue is optically cleared by a combination of urea, fructose, sucrose and thioglycerol within 12 days. Here, the suitability of combining hFRUIT and immunohistochemistry, applied to (aged) human brain tissue remains elusive. Regardless, human cytoarchitecture (Hildebrand et al., 2019; Morawski et al., 2018) can be mapped within cleared samples but mapping human myeloarchitecture still remains extremely challenging (Leuze et al., 2021).

Conclusion

Optically clearing aged human brain tissue is possible with several tissue clearing approaches. It is important to define experimental (e.g. PMD, fixation, desired immunohistochemical processing) and microscopic imaging requirements (e.g. desired resolution, FOV, hard- and software capacities) before applying clearing protocols to aged human brain tissue. Several limitations apply to the phases before, during and after clearing. These can be overcome by using and combining the CLARITY technique with high resolution microscopes, i.e. the Zeiss LSM 880. Also, the combination of the iDISCO technique with light sheet microscopes suited for wide-scale imaging, i.e. the Miltenyi BioTec UM ll, will attain sufficient tissue clearing results in aged human brain tissue.

Successfully clearing aged human brain tissue while preserving its microstructure and suitability for immunohistochemistry will be of great significance. There is growing demand for visualizing and examining human cyto- and myeloarchitecture, e.g. collecting information on cortical columns and intracortical and short white matter fibers in 3D (Attar et al., 2020; Kirilina et al., 2020). Once mastered in 3D *post mortem* human brain blocks, tools such as fiber tracking and co-localization are going to provide a powerful tool for multi-modal validation of *in vivo* microstructure-mapping using MRI.

Data availability

The data that support the findings of this study are available from the corresponding author Markus Morawski upon reasonable request.

Declaration of Competing Interest

The authors declare no personal or financial conflict of interests related to this research.

Acknowledgments

The project was founded by the Deutsche Forschungsgemeinschaft (DFG Priority Program 2041 “Computational Connectomics”, MO 2249/3-1, MO 2249/3-2, KI 1337/2-2, WE 5046/4-2) and the Alzheimer Forschungsinitiative e.V. (AFI #18072) to M.M.) as well as the DFG Emmy Noether Stipend: MO 2397/4-1 to S.M. The authors acknowledge support from the DFG and the University of Leipzig within the program of Open Access Publishing. M.B. has received funding from the International Max Planck Research School on Neuroscience of Communication: Function, Structure, and Plasticity.

The authors would like to thank Martin Grunwald and Sven Martin for providing a larger sample holder for the Ultramicroscope ll. We would like to thank Bernd Biedermann very much as well for giving technical advice. Special thanks are given to Nico Scherf and Philip Ruthig

for giving insights into data processing tools and helping with data interpretation.

Supplementary materials

Supplementary material associated with this article can be found, in the online version, at doi:10.1016/j.neuroimage.2021.118832.

References

Abe, H., Tani, T., Mashiko, H., Kitamura, N., Miyakawa, N., Mimura, K., Sakai, K., Suzuki, W., Kurotani, T., Mizukami, H., Watakabe, A., Yamamori, T., Ichinohe, N., 2017. 3D reconstruction of brain section images for creating axonal projection maps in marmosets. J. Neurosci. Methods 286, 102–113. doi:10.1016/j.jneumeth.2017.04.016.

Alkemade, A., Pine, K., Kirilina, E., Keuken, M.C., Mulder, M.J., Balesar, R., Groot, J.M., Bleys, R.L.A.W., Trampel, R., Weiskopf, N., Herrler, A., Möller, H.E., Bazin, P.-L., Forstmann, B.U., 2020. 7 Tesla MRI followed by histological 3D reconstructions in whole-brain specimens. Front. Neuroanat. 14, 536838. doi:10.3389/fnana.2020.536838.

Amunts, K., Lepage, C., Borgeat, L., Mohlberg, H., Dickscheid, T., Rousseau, M.-É., Bludau, S., Bazin, P.-L., Lewis, L.B., Oros-Peusquens, A.-M., Shah, N.J., Lippert, T., Zilles, K., Evans, A.C., 2013. BigBrain: an ultrahigh-resolution 3D human brain model. Science 340, 1472–1475. doi:10.1126/science.1235381.

Ando, K., Laborde, Q., Lazar, A., Godefroy, D., Youssef, I., Amar, M., Pooler, A., Potier, M.-.C., Delatour, B., Duyckaerts, C., 2014. Inside Alzheimer brain with CLARITY: senile plaques, neurofibrillary tangles and axons in 3-D. Acta Neuropathol. 128, 457–459. doi:10.1007/s00401-014-1322-y.

Anger, P., Bharadwaj, P., Novotny, L., 2006. Enhancement and quenching of single-molecule fluorescence. Physical review letters 96, 113002. https://doi.org/10.1103/PhysRevLett.96.113002.

Attar, F.M., Kirilina, E., Haenelt, D., Pine, K.J., Trampel, R., Edwards, L.J., Weiskopf, N., 2020. Mapping short association fibers in the early cortical visual processing stream using in vivo diffusion tractography. Cereb. Cortex 30, 4496–4514. doi:10.1093/cercor/bhaa049.

Belle, M., Godefroy, D., Couly, G., Malone, S.A., Collier, F., Giacobini, P., Chédotal, A., 2017. Tridimensional visualization and analysis of early human development. Cell 169, 161–173. doi:10.1016/j.cell.2017.03.008, e12.

de Bossolani, G.D.P., Pintelon, I., Detrez, J.D., Buckinx, R., Thys, S., Zanoni, J.N., Vos, W.H., Timmermans, .J.-P., 2019. Comparative analysis reveals Ce3D as optimal clearing method for in toto imaging of the mouse intestine. Neurogastroenterol. Motil.: Off. J. Eur. Gastrointest. Motil. Soc. 31, e13560. doi:10.1111/nmo.13560.

Brammerloh, M., Morawski, M., Friedrich, I., Reinert, T., Lange, C., Pelicon, P., Vavpetič, P., Jankuhn, S., Jäger, C., Alkemade, A., Balesar, R., Pine, K., Gavriilidis, F., Trampel, R., Reimer, E., Arendt, T., Weiskopf, N., Kirilina, E., 2021. Measuring the iron content of dopaminergic neurons in substantia nigra with MRI relaxometry. Neuroimage 239, 118255. doi:10.1016/j.neuroimage.2021.118255.

Buhl, E.H., Schlote, W., 1987. Intracellular lucifer yellow staining and electron microscopy of neurones in slices of fixed epitumourous human cortical tissue. Acta Neuropathol. 75, 140–146. doi:10.1007/BF00687074.

Bürgers, J., Pavlova, I., Rodriguez-Gatica, J.E., Henneberger, C., Oeller, M., Ruland, J.A., Siebrasse, J.P., Kubitscheck, U., Schwarz, M.K., 2019. Light-sheet fluorescence expansion microscopy: fast mapping of neural circuits at super resolution. Neurophotonics 6, 15005. doi:10.1117/1.NPh.6.1.015005.

Cartmell, S.C., Tian, Q., Thio, B.J., Leuze, C., Ye, L., Williams, N.R., Yang, G., Ben-Dor, G., Deisseroth, K., Grill, W.M., McNab, J.A., Halpern, C.H., 2019. Multimodal characterization of the human nucleus accumbens. Neuroimage doi:10.1016/j.neuroimage.2019.05.019.

Cho, I., Seo, J.Y., Chang, J., 2018. Expansion microscopy. J. Microsc. doi:10.1111/jmi.12712.

Chung, K., Wallace, J., Kim, S.-.Y., Kalyanasundaram, S., Andalman, A.S., Davidson, T.J., Mirzabekov, J.J., Zalocusky, K.A., Mattis, J., Denisin, A.K., Pak, S., Bernstein, H., Ramakrishnan, C., Grosenick, L., Gradinaru, V., Deisseroth, K., 2013. Structural and molecular interrogation of intact biological systems. Nature 497, 332–337. doi:10.1038/nature12107.

Costantini, I., Cicchi, R., Silvestri, L., Vanzi, F., Pavone, F.S., 2019. In-vivo and ex-vivo optical clearing methods for biological tissues: review. Biomed. Opt. Express 10, 5251–5267. doi:10.1364/BOE.10.005251.

Costantini, I., Ghobril, J.-.P., Di Giovanna, A.P., Allegra Mascaro, A.L., Silvestri, L., Müllenbroich, M.C., Onofri, L., Conti, V., Vanzi, F., Sacconi, L., Guerrini, R., Markram, H., Iannello, G., Pavone, F.S., 2015. A versatile clearing agent for multi-modal brain imaging. Sci. Rep. 5, 1–9. doi:10.1038/srep09808.

Dodt, H.-.U., Leischner, U., Schierloh, A., Jährling, N., Mauch, C.P., Deininger, K., Deussing, J.M., Eder, M., Zieglgänsberger, W., Becker, K., 2007. Ultramicroscopy: three-dimensional visualization of neuronal networks in the whole mouse brain. Nat. Methods 4, 331–336. doi:10.1038/nmeth1036.

Duncan, Arlene, Meek H, Judith, Clemence, Matthew, Elwell E, Clare, Fallon, Penny, Tyszczuk, Lidia, Cope, Mark, Delpy T, David, 1996. Measurement of Cranial Optical Path Length as a Function of Age Using Phase Resolved Near Infrared Spectroscopy. Pediatric Research 889–894.

Edwards, L.J., Kirilina, E., Mohammadi, S., Weiskopf, N., 2018. Microstructural imaging of human neocortex in vivo. Neuroimage 182, 184–206. doi:10.1016/j.neuroimage.2018.02.055.

Gómez-Gaviro, M.V., Sanderson, D., Ripoll, J., Desco, M., 2020. Biomedical applications of tissue clearing and three-dimensional imaging in health and disease. iScience 23, 101432. doi:10.1016/j.isci.2020.101432.

Goyal, V., 1982. Lipofuscin pigment accumulation in human brain during aging. Exp. Gerontol. 17, 481–487. doi:10.1016/S0531-5565(82)80010-7.

Hahn, M., Nord, C., Franklin, O., Alanentalo, T., Mettävainio, M.I., Morini, F., Eriksson, M., Korsgren, O., Sund, M., Ahlgren, U., 2020. Mesoscopic 3D imaging of pancreatic cancer and Langerhans islets based on tissue autofluorescence. Sci. Rep. 10, 18246. doi:10.1038/s41598-020-74616-6.

Hellwig, B., 1993. How the myelin picture of the human cerebral cortex can be computed from cytoarchitectural data. A bridge between von Economo and Vogt. J. Hirnforsch. 34, 387–402.

Helmstaedter, M., 2013. Cellular-resolution connectomics: challenges of dense neural circuit reconstruction. Nat. Methods 10, 501–507. doi:10.1038/nmeth.2476.

Helmstaedter, M., Briggman, K.L., Denk, W., 2011. High-accuracy neurite reconstruction for high-throughput neuroanatomy. Nat. Neurosci. 14, 1081–1088. doi:10.1038/nn.2868.

Helmstaedter, M., Mitra, P.P., 2012. Computational methods and challenges for large-scale circuit mapping. Curr. Opin. Neurobiol. 22, 162–169. doi:10.1016/j.conb.2011.11.010.

Hildebrand, S., Schueth, A., Herrler, A., Galuske, R., Roebroeck, A., 2019. Scalable labeling for cytoarchitectonic characterization of large optically cleared human neocortex samples. Sci. Rep. 9, 10880. doi:10.1038/s41598-019-47336-9.

Hildebrand, S., Schueth, A., Wangenheim, K.von, Mattheyer, C., Pampaloni, F., Bratzke, H., Roebroeck, A.F., Galuske, R.A.W., 2020. hFRUIT: an optimized agent for optical clearing of DiI-stained adult human brain tissue. Sci. Rep. 10, 9950. doi:10.1038/s41598-020-66999-3.

Hou, B., Zhang, D., Zhao, S., Wei, M., Yang, Z., Wang, S., Wang, J., Zhang, X., Liu, B., Fan, L., Li, Y., Qiu, Z., Zhang, C., Jiang, T., 2015. Scalable and DiI-compatible optical clearance of the mammalian brain. Front. Neuroanat. 9, 19. doi:10.3389/fnana.2015.00019.

Jacques, S.L., 2013. Optical properties of biological tissues: a review. Phys. Med. Biol. 58, R37–R61. doi:10.1088/0031-9155/58/11/R37.

Jing, D., Zhang, S., Luo, W., Gao, X., Men, Y., Ma, C., Liu, X., Yi, Y., Bugde, A., Zhou, B.O., Zhao, Z., Yuan, Q., Feng, J.Q., Gao, L., Ge, W.-.P., Zhao, H., 2018. Tissue clearing of both hard and soft tissue organs with the PEGASOS method. Cell Res. 28, 803. doi:10.1038/s41422-018-0049-z.

Johansson, J.D., 2010. Spectroscopic method for determination of the absorption coefficient in brain tissue. JBO 15, 57005. doi:10.1117/1.3495719.

Johnsen, Widder, 1999. The physical basis of transparency in biological tissue: ultrastructure and the minimization of light scattering. J. Theor. Biol. 199, 181–198. doi:10.1006/jtbi.1999.0948.

Kaas, J.H., 2012. Evolution of columns, modules, and domains in the neocortex of primates. Proc. Natl. Acad. Sci. U.S.A. 109 (Suppl 1), 10655–10660. doi:10.1073/pnas.1201892109.

Kerker, M., 1969. The Scattering of Light and Other Electromagnetic Radiation. Academic Press, Potsdam, NY, p. 688.

Kim, J.H., Jang, M.J., Choi, J., Lee, E., Song, K.-.D., Cho, J., Kim, K.-.T., Cha, H.-.J., Sun, W., 2018. Optimizing tissue-clearing conditions based on analysis of the critical factors affecting tissue-clearing procedures. Sci. Rep. 8, 12815. doi:10.1038/s41598-018-31153-7.

Kirilina, E., Helbling, S., Morawski, M., Pine, K., Reimann, K., Jankuhn, S., Dinse, J., Deistung, A., Reichenbach, J.R., Trampel, R., Geyer, S., Müller, L., Jakubowski, N., Arendt, T., Bazin, P.-.L., Weiskopf, N., 2020. Superficial white matter imaging: contrast mechanisms and whole-brain in vivo mapping. Sci. Adv. 6. doi:10.1126/sciadv.aaz9281.

Klingberg, A., Hasenberg, A., Ludwig-Portugall, I., Medyukhina, A., Männ, L., Brenzel, A., Engel, D.R., Figge, M.T., Kurts, C., Gunzer, M., 2017. Fully automated evaluation of total glomerular number and capillary tuft size in nephritic kidneys using lightsheet microscopy. J. Am. Soc. Nephrol. 28, 452–459. doi:10.1681/ASN.2016020232.

Kubota, S.I., Takahashi, K., Nishida, J., Morishita, Y., Ehata, S., Tainaka, K., Miyazono, K., Ueda, H.R., 2017. Whole-body profiling of cancer metastasis with single-cell resolution. Cell Rep. 20, 236–250. doi:10.1016/j.celrep.2017.06.010.

Lai, H.M., Liu, A.K.L., Ng, H.H.M., Goldfinger, M.H., Chau, T.W., DeFelice, J., Tilley, B.S., Wong, W.M., Wu, W., Gentleman, S.M., 2018. Next generation histology methods for three-dimensional imaging of fresh and archival human brain tissues. Nat. Commun. 9, 1066. doi:10.1038/s41467-018-03359-w.

Lakowicz, J.R., 1983a. Introduction to fluorescence. Chapter 1. In: Lakowicz, J.R. (Ed.), Principles of Fluorescence Spectroscopy. Springer US, Boston, MA, pp. 1–26.

Lakowicz, J.R., 1983b. Quenching of fluorescence. In: Lakowicz, J.R. (Ed.), Principles of Fluorescence Spectroscopy. Springer US, Boston, MA, pp. 257–301.

Leuze, C., Goubran, M., Barakovic, M., Aswendt, M., Tian, Q., Hsueh, B., Crow, A., Weber, E.M.M., Steinberg, G.K., Zeineh, M., Plowey, E.D., Daducci, A., Innocenti, G., Thiran, J.-.P., Deisseroth, K., McNab, J.A., 2021. Comparison of diffusion MRI and CLARITY fiber orientation estimates in both gray and white matter regions of human and primate brain. Neuroimage 228, 117692. doi:10.1016/j.neuroimage.2020.117692.

Li, W., Germain, R.N., Gerner, M.Y., 2017. Multiplex, quantitative cellular analysis in large tissue volumes with clearing-enhanced 3D microscopy (Ce3D). Proc. Natl. Acad. Sci. U.S.A. 114, E7321–E7330. doi:10.1073/pnas.1708981114.

Liu, A.K.L., Hurry, M.E.D., Ng, O.T.W., DeFelice, J., Lai, H.M., Pearce, R.K.B., Wong, G.T.-C., Chang, R.C.-C., Gentleman, S.M., 2016. Bringing CLARITY to the human brain: visualization of Lewy pathology in three dimensions. Neuropathol. Appl. Neurobiol. 42, 573–587. doi:10.1111/nan.12293.

Liu, A.K.L., Lai, H.M., Chang, R.C.-C., Gentleman, S.M., 2017. Free of acrylamide sodium dodecyl sulphate (SDS)-based tissue clearing (FASTClear): a novel protocol of tis-

sue clearing for three-dimensional visualization of human brain tissues. Neuropathol. Appl. Neurobiol. 43, 346–351. doi:10.1111/nan.12361.

Masselink, W., Reumann, D., Murawala, P., Pasierbek, P., Taniguchi, Y., Knoblich, J.A., Tanaka, E.M., 2018. Broad applicability of a streamlined ethyl cinnamate-based clearing procedure, 26 pp.

Merz, G., Schwenk, V., Shah, R., Salafia, C., Necaise, P., Joyce, M., Villani, T., Johnson, M., Crider, N., 2018. Three-dimensional rendering and analysis of immunolabeled, clarified human placental villous vascular networks. J. Vis. Exp. e57099. doi:10.3791/57099.

Monici, M., 2005. In: Cell and Tissue Autofluorescence Research and Diagnostic Applications, vol. 11. Elsevier, pp. 227–256.

Morawski, M., Brückner, M.K., Riederer, P., Brückner, G., Arendt, T., 2004. Perineuronal nets potentially protect against oxidative stress. Exp. Neurol. 188, 309–315. doi:10.1016/j.expneurol.2004.04.017.

Morawski, M., Kirilina, E., Scherf, N., Jäger, C., Reimann, K., Trampel, R., Gavriilidis, F., Geyer, S., Biedermann, B., Arendt, T., Weiskopf, N., 2018. Developing 3D microscopy with CLARITY on human brain tissue: towards a tool for informing and validating MRI-based histology. Neuroimage 182, 417–428. doi:10.1016/j.neuroimage.2017.11.060.

Murray, E., Cho, J.H., Goodwin, D., Ku, T., Swaney, J., Kim, S.-Y., Choi, H., Park, Y.-.G., Park, J.-Y., Hubbert, A., McCue, M., Vassallo, S., Bakh, N., Frosch, M.P., van Wedeen, J., Seung, H.S., Chung, K., 2015. Simple, scalable proteomic imaging for high-dimensional profiling of intact systems. Cell 163, 1500–1514. doi:10.1016/j.cell.2015.11.025.

Nojima, S., Susaki, E.A., Yoshida, K., Takemoto, H., Tsujimura, N., Iijima, S., Takachi, K., Nakahara, Y., Tahara, S., Ohshima, K., Kurashige, M., Hori, Y., Wada, N., Ikeda, J.-I., Kumanogoh, A., Morii, E., Ueda, H.R., 2017. CUBIC pathology: three-dimensional imaging for pathological diagnosis. Sci. Rep. 7, 9269. doi:10.1038/s41598-017-09117-0.

Park, Y.-G., Sohn, C.H., Chen, R., McCue, M., Yun, D.H., Drummond, G.T., Ku, T., Evans, N.B., Oak, H.C., Trieu, W., Choi, H., Jin, X., Lilascharoen, V., Wang, J., Truttmann, M.C., Qi, H.W., Ploegh, H.L., Golub, T.R., Chen, S.-.C., Frosch, M.P., Kulik, H.J., Lim, B.K., Chung, K., 2018. Protection of tissue physicochemical properties using polyfunctional crosslinkers. Nat. Biotechnol. 37, 73–83. doi:10.1038/nbt.4281.

Perin, P., Voigt, F.F., Bethge, P., Helmchen, F., Pizzala, R., 2019. iDISCO+ for the study of neuro-immune architecture of the rat auditory brainstem. Front. Neuroanat. 13, 15. doi:10.3389/fnana.2019.00015.

Renier, N., Adams, E.L., Kirst, C., Wu, Z., Azevedo, R., Kohl, J., Autry, A.E., Kadiri, L., Umadevi Venkataraju, K., Zhou, Y., Wang, V.X., Tang, C.Y., Olsen, O., Dulac, C., Osten, P., Tessier-Lavigne, M., 2016. Mapping of brain activity by automated volume analysis of immediate early genes. Cell 165, 1789–1802. doi:10.1016/j.cell.2016.05.007.

Renier, N., Wu, Z., Simon, D.J., Yang, J., Ariel, P., Tessier-Lavigne, M., 2014. iDISCO: a simple, rapid method to immunolabel large tissue samples for volume imaging. Cell 159, 896–910. doi:10.1016/j.cell.2014.10.010.

Richardson, D.S., Lichtman, J.W., 2015. Clarifying tissue clearing. Cell 162, 246–257. doi:10.1016/j.cell.2015.06.067.

Sabdyusheva Litschauer, I., Becker, K., Saghafi, S., Ballke, S., Bollwein, C., Foroughipour, M., Gaugeler, J., Foroughipour, M., Schavelová, V., László, V., Döme, B., Brostjan, C., Weichert, W., Dodt, .H..-U., 2020. 3D histopathology of human tumours by fast clearing and ultramicroscopy. Sci. Rep. 10, 17619. doi:10.1038/s41598-020-71737-w.

Sele, M., Wernitznig, S., Lipovšek, S., Radulović, S., Haybaeck, J., Birkl-Toeglhofer, A.M., Wodlej, C., Kleinegger, F., Sygulla, S., Leoni, M., Ropele, S., Leitinger, G., 2019. Optimization of ultrastructural preservation of human brain for transmission electron microscopy after long post-mortem intervals. Acta Neuropathol. Commun. 7, 144. doi:10.1186/s40478-019-0794-3.

Silvestri, L., Costantini, I., Sacconi, L., Pavone, F.S., 2016. Clearing of fixed tissue: a review from a microscopist's perspective. J. Biomed. Opt. 21, 81205. doi:10.1117/1.JBO.21.8.081205.

Spalteholz, W., 1914. Über das Durchsichtigmachen von menschlichen und tierischen Präparaten und seine theoretischen Bedingungen, 1–47.

Stan, A.D., Ghose, S., Gao, X.-.M., Roberts, R.C., Lewis-Amezcua, K., Hatanpaa, K.J., Tamminga, C.A., 2006. Human postmortem tissue: what quality markers matter? Brain Res. 1123, 1–11. doi:10.1016/j.brainres.2006.09.025.

Struzyna, L.A., Browne, K.D., Brodnik, Z.D., Burrell, J.C., Harris, J.P., Chen, H.I., Wolf, J.A., Panzer, K.V., Lim, J., Duda, J.E., España, R.A., Cullen, D.K., 2018. Tissue engineered nigrostriatal pathway for treatment of Parkinson's disease. J. Tissue Eng. Regen. Med. 12, 1702–1716. doi:10.1002/term.2698.

Susaki, E.A., Tainaka, K., Perrin, D., Yukinaga, H., Kuno, A., Ueda, H.R., 2015. Advanced CUBIC protocols for whole-brain and whole-body clearing and imaging. Nat. Protoc. 10, 1709–1727. doi:10.1038/nprot.2015.085.

Tian, T., Yang, Z., Li, X., 2020. Tissue clearing technique: recent progress and biomedical applications. J. Anat. doi:10.1111/joa.13309.

Tuchin, V.V., 2015. Tissue optics and photonics: light-tissue interaction. JBPE 98–134. doi:10.18287/JBPE-2015-1-2-98.

Ueda, H.R., Ertürk, A., Chung, K., Gradinaru, V., Chédotal, A., Tomancak, P., Keller, P.J., 2020. Tissue clearing and its applications in neuroscience. Nat. Rev. Neurosci. 21, 61–79. doi:10.1038/s41583-019-0250-1.

Villani, T.S., Koroch, A.R., Simon, J.E., 2013. An improved clearing and mounting solution to replace chloral hydrate in microscopic applications. Appl. Plant Sci. 1. doi:10.3732/apps.1300016.

Weiskopf, N., Edwards, L., Helms, G., Mohammadi, S., Kirilina, E., 2021. Quantitative magnetic resonance imaging of brain anatomy and in-vivo histology. Nat. Rev. Phys..

Weissleder, R., 2001. A clearer vision for in vivo imaging. Nat. Biotechnol. 19, 316–317. doi:10.1038/86684.

Zhanmu, O., Yang, X., Gong, H., Li, X., 2020. Paraffin-embedding for large volume biotissue. Sci. Rep. 10, 12639. doi:10.1038/s41598-020-68876-5.

Zhao, S., Todorov, M.I., Cai, R., Steinke, H., Kemter, E., Wolf, E., Lipfert, J., Bechmann, I., Ertürk, A., 2019. Cellular and molecular probing of intact transparent human organs, 28 pp.